Characteristics of small-scale shear layers in a temporally evolving turbulent planer jet

Masato Hayashi, [1] Tomoaki Watanabe[2]† and Koji Nagata[2]

[1]Department of Mechanical Systems Engineering, Nagoya University, Nagoya 464-8603, Japan
[2]Department of Aerospace Engineering, Nagoya University, Nagoya 464-8603, Japan

(Received xx; revised xx; accepted xx)

Characteristics of small-scale shear layers are studied with direct numerical simulations of a temporally evolving turbulent planar jet. The shear layers that internally exist in turbulence are detected with a tensor of shearing motion, which is extracted from a velocity gradient tensor with a triple decomposition. Flow visualization of the shear intensity confirms the existence of layer structures with intense shear. The mean flow characteristics around local maxima of the shear intensity are investigated with averages taken in the shear coordinate system, which is defined based on the shear orientation. The mean flow pattern reveals that the shear layer is formed in a biaxial strain field, which consists of extensive strain in the vorticity direction of the shear and compressive strain in the direction perpendicular to the shear layer. The velocity components associated with the shear and biaxial strain rapidly change around the shear layer. The Kolmogorov scales characterize the mean characteristics of shear layers, such as velocity jumps, thickness and the intensities of shear and biaxial strain. These quantities normalized by the Kolmogorov scales only weakly depend on lateral positions in the planar jet. Although the turbulent planar jet evolves under the influence of mean shear, a large number of the shear layers do not align with the mean shear direction. The typical shear layer thickness is about 6 times the Kolmogorov length scale. Furthermore, the shear layer thickness is well predicted by Burgers' vortex layer.

1. Introduction

Turbulence comprises intricate fluid motions with a wide range of characteristic length scales and governs various phenomena in physics and engineering (Davidson 2004). For example, it is known that turbulence enhances mixing and diffusion, and the rate of turbulent mixing of heat, momentum and energy is crucial in engineering application, such as chemical reactors (Ghanem *et al.* 2014) and combustion devices (Veynante & Vervisch 2002). Turbulent motions at small scales are related to many important features of turbulence. Dissipation of turbulent kinetic energy is associated with small-scale velocity fluctuations. Diffusion of fluid mixtures also efficiently occurs at small scales. Therefore, understanding the small-scale properties of turbulence is expected to provide some insight into the development of physical and numerical models of turbulent flows (Meneveau 2011).

Turbulence is often studied in terms of coherent structures, which can be identified

† Email address for correspondence: watanabe.tomoaki@c.nagoya-u.jp

by flow visualization as their characteristic patterns. Turbulence has also been studied with various statistics. The approach based on turbulent structures is often compared with that based on statistics. For example, in the statistical approach, small-scale characteristics of turbulence can be studied with the scaling exponents for structure functions (Kholmyansky *et al.* 2001). On the other hand, the spatiotemporal distributions of small-scale quantities, such as enstrophy and energy dissipation rate, often display the structures underlying their statistical features (Siggia 1981; Jiménez *et al.* 1993). Statistical and structural approaches are not incompatible with each other, and they help us understand the physics of turbulence from different aspects as discussed in Tsinober (2009).

Physical variables defined with a velocity gradient tensor $\nabla \boldsymbol{u}$ are widely used to identify small-scale structures of turbulence. In this study, a component of a second-order tensor is specified with subscripts, e.g. $(\nabla \boldsymbol{u})_{ij} = \partial u_i/\partial x_j$. In incompressible flows, the velocity gradient tensor is often decomposed into symmetric and anti-symmetric parts, which are called a rate-of-strain tensor $S_{ij} = [(\nabla \boldsymbol{u})_{ij} + (\nabla \boldsymbol{u})_{ji}]/2$ and a rate-of-rotation tensor $\Omega_{ij} = [(\nabla \boldsymbol{u})_{ij} - (\nabla \boldsymbol{u})_{ji}]/2$, respectively. Non-zero components of Ω_{ij} are proportional to components of a vorticity vector $\boldsymbol{\omega} = \nabla \times \boldsymbol{u}$, and enstrophy $\omega^2/2$ is expressed as $\omega^2/2 \equiv \boldsymbol{\omega} \cdot \boldsymbol{\omega}/2 = \Omega_{ij}\Omega_{ij}$, where summation is taken for the repeated indices i and j. The enstrophy is often used to explore small-scale vorticity structures. Visualization of regions with large enstrophy revealed the existence of small-scale tubular vortices, which are often called vortex tubes, worms or filaments (Siggia 1981; Yamamoto & Hosokawa 1988; Jimenez & Wray 1998). The vortex tubes can also be detected with the second invariant of the velocity gradient tensor $Q = (\Omega_{ij}\Omega_{ij} - S_{ij}S_{ij})/2$. The characteristics of vortex tubes have been studied in various turbulent flows (Kang *et al.* 2007; Pirozzoli *et al.* 2008; da Silva *et al.* 2011; Jahanbakhshi *et al.* 2015). These studies have shown that the typical diameter and azimuthal velocity of vortex tubes scale with the Kolmogorov length and velocity scales, respectively, and the vortex tubes in turbulence are considered to have some universal properties.

Besides the vortex tubes, sheetlike vortices (vortex sheets or vortex layers) with moderately large enstrophy also exist in turbulent flows (Ruetsch & Maxey 1991; Jimenez & Wray 1998). The vortex sheets are formed in regions with intense shear, where S_{ij} is comparable to Ω_{ij}. Therefore, the vortex sheets are also called shear layers or internal shear layers (Eisma *et al.* 2015; Watanabe *et al.* 2020; Gul *et al.* 2020). Several methods have been proposed to detect the location of vortex sheets in a three-dimensional velocity field in turbulence (Horiuti 2001; Horiuti & Takagi 2005; Pirozzoli *et al.* 2010). The analysis of flow regions occupied by vortex sheets showed that the vortex sheets play important roles in dynamics of turbulence, such as energy dissipation rate, enstrophy production due to vortex stretching and self-amplification of strain (Tsinober 2009). It was also shown that the roll-up of shear layers causes the formation of vortex tubes (Vincent & Meneguzzi 1994; Watanabe *et al.* 2020).

The geometry and local flow topology of vortex tubes have been studied by identifying the axis of the vortex tubes with a vorticity vector (Jiménez *et al.* 1993), which can be used to define the axial, azimuthal and radial directions. The analysis of vortex tubes concerning these directions revealed that the vortex tubes are stretched by axial strain (Jimenez & Wray 1998; da Silva *et al.* 2011), where the relation between the diameter of vortex tubes and the intensity of the axial strain was well predicted by Burgers' vortex. Unfortunately, classical identification schemes of vortex sheets hardly provide information on the orientation of the vortex sheets, and the geometrical and topological properties of vortex sheets are less understood than the vortex tubes.

Recently, a new method has been developed for detecting vortex sheets based on a triple

decomposition of the velocity gradient tensor (Kolář 2007), which decomposes $(\nabla \boldsymbol{u})_{ij}$ into three components representing motions of shear, rotation and elongation. Since this method identifies the vortex sheets with the local intensity of shearing motion, the vortex sheets detected with the triple decomposition are called shear layers in this study. The triple decomposition was firstly developed for the detection of vortex tubes (Kolář 2007). However, it proved to be useful in the detection of vortex sheets in turbulent flows (Maciel *et al.* 2012). The triple decomposition was originally formulated for 3×3 components of the velocity gradient tensor. However, most studies applied the triple decomposition to two-dimensional components of the velocity gradient tensor, $(\nabla \boldsymbol{u})_{ij}$ with $i, j = 1$ and 2, where the decomposed tensors represent three motions on a two-dimensional plane (Maciel *et al.* 2012; Eisma *et al.* 2015). This is because the algorithm of the decomposition is much simpler for the two-dimensional velocity gradient tensor (Kolář 2007). Eisma *et al.* (2015) investigated shear layers in a turbulent boundary layer by applying the triple decomposition of two-dimensional components of the velocity gradient tensor, and observed a velocity jump around regions with intense shear. In our previous study, a numerical algorithm of the triple decomposition for the full velocity gradient tensor $(\nabla \boldsymbol{u})_{ij}$ with $i, j = 1, 2$ and 3 was developed and tested with direct numerical simulation (DNS) databases of homogeneous isotropic turbulence (Nagata *et al.* 2020). This method was used to investigate the shear layers in homogeneous isotropic turbulence in Watanabe *et al.* (2020), where the shear layer orientation was successfully identified with the tensor representing shearing motion. Analysis of a three-dimensional velocity field in relation to the shear layer orientation showed that the shear layer is sustained by a biaxial strain field. It was also shown that three-dimensionality is important in the flow topology around the shear layer although the shear itself can be expressed on a two-dimensional plane.

Analysis of shear layers with the triple decomposition of the three-dimensional velocity gradient tensor was reported only for homogeneous isotropic turbulence. It is expected that the recent technique to detect shear layers is applied to various turbulent flows to reveal the universality and flow dependence of shear layers. In this study, the shear layer analysis based on the triple decomposition is conducted with DNS databases of an incompressible, temporally evolving turbulent planar jet (Watanabe *et al.* 2019). We compare the characteristics of shear layers obtained with the triple decomposition between the turbulent planar jet and homogeneous isotropic turbulence in order to assess the effects of mean velocity gradient of the jet, which are absent in homogeneous isotropic turbulence. The paper is organized as follows. § 2 describes DNS of the temporally evolving turbulent planar jet. § 3 presents the details of the triple decomposition and the shear layer analysis. DNS results are discussed in § 4 with a special focus on the characteristics of shear layers. Finally, the paper is summarized in § 5.

2. DNS of a temporally evolving turbulent planar jet

2.1. *DNS databases*

We analyse DNS databases of a temporally evolving turbulent planar jet with a passive scalar transfer. Temporally evolving turbulent shear flows have often been investigated as an approximation of spatially evolving counterparts. For examples, temporal simulations were used for boundary layers, jets, wakes and mixing layers (Moser *et al.* 1998; Rogers & Moser 1994; da Silva & Pereira 2008; Diamessis *et al.* 2011; Gampert *et al.* 2014; van Reeuwijk & Holzner 2014; Kozul *et al.* 2016; Watanabe *et al.* 2018*b*; Sadeghi *et al.* 2018), where differences and similarities between temporal and spatial simulations were

discussed. One of the differences is the interaction between different streamwise locations, which occurs only in the spatial jet. The purpose of this study is to investigate shear layers in turbulence evolving under the influence of mean shear. For this purpose, the temporally evolving planar jet is adequate as a higher Reynolds number can be achieved at a reasonable computational cost in temporal simulations than in spatial simulations. A transverse profile of mean streamwise velocity hardly differs between temporal and spatial jets (da Silva & Pereira 2008; van Reeuwijk & Holzner 2014; Watanabe *et al.* 2018*b*), and the mean shear effects on the small-scale shear layers are also expected to be similar in these flows.

The temporally evolving planar jet develops with time in a computational domain which is periodic in the streamwise and spanwise directions (da Silva & Pereira 2008). The jet Reynolds number is defined with an initial jet velocity U_J and a width H as $Re_J = U_J H/\nu$, where ν is the kinematic viscosity. The Schmidt number $Sc = \nu/D$ is assumed to be one, where D is the diffusivity coefficient of the passive scalar. Streamwise, lateral and spanwise directions of the planar jet are represented by x, y and z, respectively, and the corresponding components of the velocity vector are u, v and w. The temporally evolving planar jet is statistically homogeneous in the x and z directions. Therefore, statistics are obtained by taking averages on a x-z plane as functions of y and time t. This average is denoted by $\langle\,\rangle$ while fluctuations of a variable f are defined as $f' = f - \langle f \rangle$.

DNS databases for $Re_J = 10000$, 40000 and 100000 in Watanabe *et al.* (2019) are used in this study. Besides, we have performed DNS for $Re_J = 4000$ with the same DNS code. Results of the DNS except for $Re_J = 4000$ were reported in Watanabe *et al.* (2019), where good agreement between the DNS and other numerical and experimental studies was found for mean velocity, root-mean-squared (rms) velocity fluctuations in three directions, mean scalar, rms scalar fluctuations, energy spectra, Reynolds number dependence of derivative skewness and flatness and the auto-correlation function of streamwise velocity fluctuations. The DNS code was also used in our previous studies on mixing layers and boundary layers (Watanabe *et al.* 2018*a*,*b*), where DNS results were compared well with experiments and other DNS. The code is briefly described in this section.

The governing equations are the incompressible Navier–Stokes equations and an advection-diffusion equation for the passive scalar ϕ (e.g. a mass fraction of dilute and inert gas):

$$\frac{\partial u_j}{\partial x_j} = 0, \tag{2.1}$$

$$\frac{\partial u_i}{\partial t} + \frac{\partial u_i u_j}{\partial x_j} = -\frac{1}{\rho}\frac{\partial p}{\partial x_i} + \nu \frac{\partial^2 u_i}{\partial x_j \partial x_j}, \tag{2.2}$$

$$\frac{\partial \phi}{\partial t} + \frac{\partial \phi u_j}{\partial x_j} = D \frac{\partial^2 \phi}{\partial x_j \partial x_j}, \tag{2.3}$$

where u_i is the i-th component of the velocity vector, p is the pressure and ρ is a constant value of the fluid density. These equations are solved with the DNS code based on the fractional step method. Periodic boundary conditions are applied in the x and z directions. The boundaries in the y direction are treated with free slip boundary conditions. Spatial derivatives are computed with fully conservative central difference schemes (Morinishi *et al.* 1998), where the second-order and fourth-order schemes are used in the lateral direction and other directions, respectively. Time is advanced with a third-order Runge-Kutta method. The Bi-CGSTAB method is used to solve the Poisson equation for pressure.

The initial mean velocity profile of the temporally evolving turbulent planar jet is given with a hyperbolic tangent function (da Silva & Pereira 2008):

$$\langle u \rangle = \frac{1}{2}U_J + \frac{1}{2}U_J \tanh\left(\frac{H - 2|y|}{4\theta_J}\right), \quad \langle v \rangle = \langle w \rangle = 0, \tag{2.4}$$

with $\theta_J = 0.01H$. The centre of the jet is located at $y = 0$. The initial velocity field consists of the mean velocity and spatially correlated random fluctuations (Watanabe *et al.* 2019), where fluctuations with rms values of $0.025U_J$ are added in the region of $|y| \leqslant 0.5H$. The initial profile of ϕ is given by

$$\phi = \frac{1}{2}\phi_J + \frac{1}{2}\phi_J \tanh\left(\frac{H - 2|y|}{4\theta_J}\right), \tag{2.5}$$

where $\phi = \phi_J$ and 0 in the jet and ambient fluid, respectively. The DNS code solves the governing equations non-dimensionalized by U_J, H and ϕ_J.

The DNS uses the computational domain with the size of $(L_x \times L_y \times L_z) = (6H \times 10H \times 4H)$. In a temporally evolving planar jet with this computational domain, the longitudinal auto-correlation function defined with the streamwise separation distance is consistent with DNS results of a spatially evolving turbulent planar jet as reported in Watanabe *et al.* (2019). Therefore, the computational domain is large enough to prevent unphysical effects of the periodic boundary conditions applied in the streamwise direction. The summary of DNS is presented in table 1, which contains the number of grid points $(N_x \times N_y \times N_z)$. The grid points are uniformly spaced in the x and z directions, while the grid is stretched in the y direction as $|y|$ increases using a mapping function given by

$$y(j) = -\frac{L_y}{2\alpha_y} \text{atanh}\left[(\tanh\alpha_y)\left(1 - 2\left(\frac{j-1}{N_y - 1}\right)\right)\right] \quad \text{with} \quad j = 1, ..., N_y, \tag{2.6}$$

with the grid stretching parameter $\alpha_y = 1.5$. In each simulation, time t is advanced until $t = 20t_r$, where $t_r = H/U_J$ is the reference time scale of the jet. The turbulent jet has fully developed by this time as examined below. DNS for each Re_J is repeated N_S times with different initial velocity fluctuations, where N_S is provided in table 1. Ensemble averages are taken for N_S simulations to improve statistical convergence. As shown below, the shear layers are small-scale structures, whose length scale decreases with Re_J, and the number density of shear layers increases with the Reynolds number. Therefore, the number of statistical samples in the shear layer analysis in one simulation decreases as Re_J becomes small. For this reason, N_S is larger for lower Reynolds number cases. N_S is determined such that the mean velocity profile around shear layers examined in § 4.3 is well converged.

2.2. *Characteristics of the temporally evolving turbulent planar jet*

Figure 1 visualizes the development of the planar jet at $Re_J = 4000$ and 40000 with two-dimensional profiles of ϕ at four time instances. Turbulence is generated at the edges of the jet at $t = 5t_r$ and spreads in the lateral direction with time. The jet core region has $\phi/\phi_J = 1$ at early time while the jet development is accompanied by the mixing of the jet and ambient fluids, which results in $\phi/\phi_J < 1$ even in the central region of the jet at late time. The jet has already fully developed at $t = 15t_r$ as attested by small-scale scalar fluctuations that occupy the entire jet region. Although the initial mean velocity profile is the same in all simulations, the turbulent transition of the planar jet depends on the Reynolds number. At $Re_J = 40000$, small-scale fluctuations exist inside the roller vortices arising from the Kelvin-Helmholtz instability in figure 1(f) while they are absent at $Re_J = 4000$ in figure 1(b). We have also confirmed that pairing of multiple

Table 1: Computational and physical parameters of DNS. The statistics shown in the table are taken at $t = 20t_r$. Δ_y, η, λ and Re_λ are obtained at $y = 0$.

Re_J	N_S	N_x	N_y	N_z	Δ_x/η	Δ_y/η	Δ_z/η	η/H	λ/H	b_u/H	Re_λ
4000	9	432	600	288	1.5	1.1	1.5	0.0089	0.13	0.98	59
10000	6	864	1200	576	1.6	1.2	1.6	0.0046	0.089	0.91	97
40000	3	2304	3200	1536	1.5	1.1	1.5	0.0016	0.045	0.88	215
100000	1	4608	5800	3072	1.7	1.3	1.7	0.00077	0.028	0.81	336

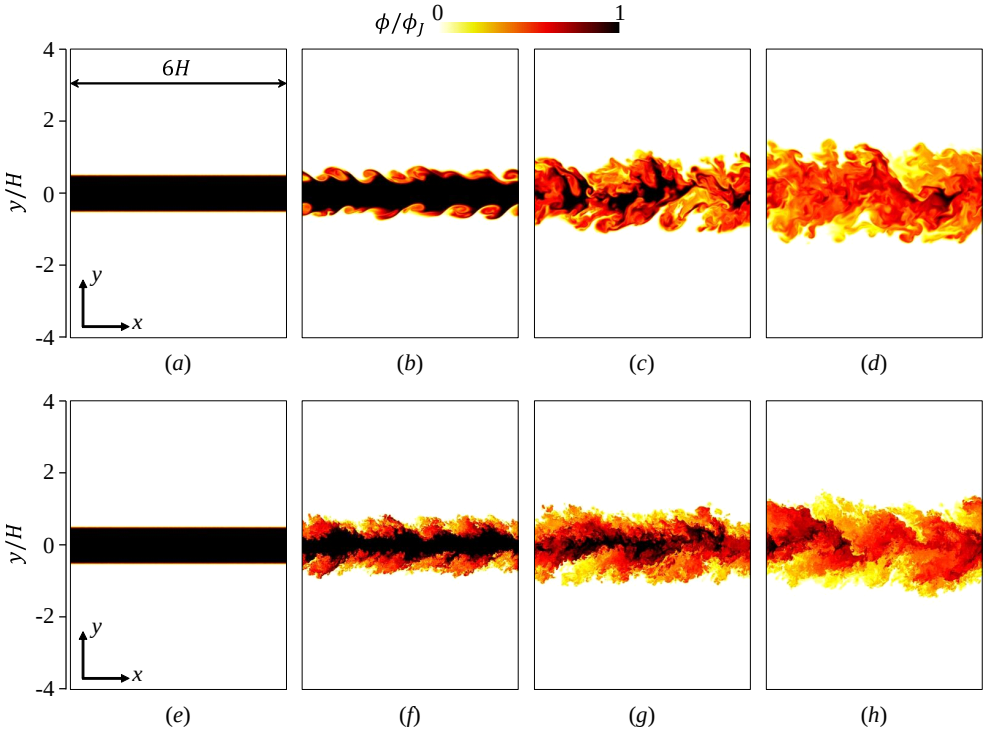

Figure 1: Development of the temporally evolving turbulent planar jet with (*a-d*) $Re_J = 4000$ and (*e-h*) $Re_J = 40000$. Passive scalar ϕ is visualized on a x-y plane at (a, e) $t/t_r = 0$, (b, f) $t/t_r = 5$, (c, g) $t/t_r = 10$ and (d, h) $t/t_r = 15$.

roller vortices occurs before $t/t_r = 5$ at $Re_J = 4000$ (not shown in figure 1). Then, as the roller vortices grow with time, the interaction of the vortices on both sides of the jet results in the formation of the fully developed turbulent jet. However, three-dimensional velocity and scalar fluctuations already develop inside the roller vortices at $Re_J = 40000$, and turbulent mixing layers are formed at the edges of the jet before the turbulent jet develops. Then, the growth of the turbulent mixing layers results in the development of the turbulent jet at high Re_J.

Figure 2 shows the lateral profiles of mean streamwise velocity $\langle u \rangle$ and rms streamwise

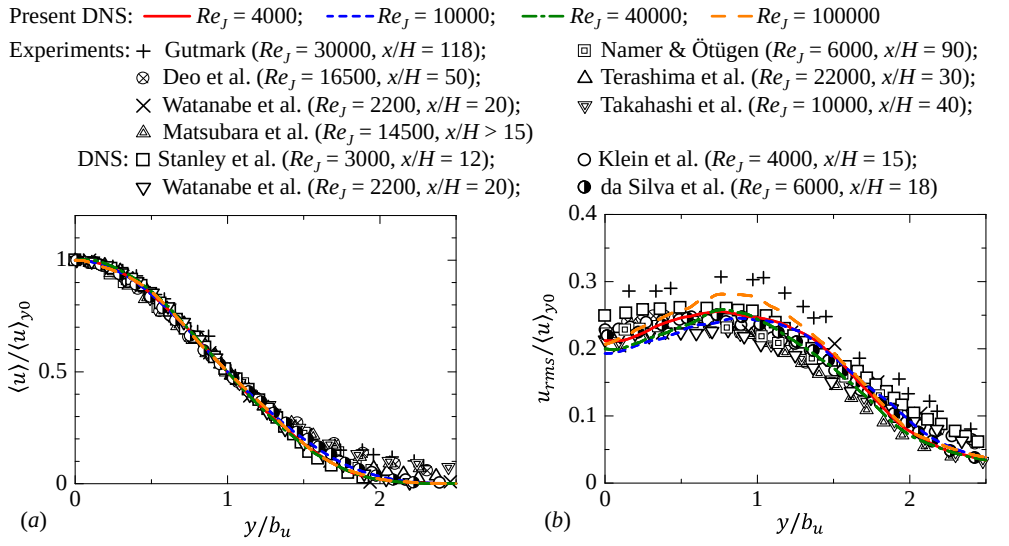

Figure 2: Lateral profiles of (a) mean streamwise velocity $\langle u\rangle$ and (b) root-mean-squared streamwise velocity fluctuations u_{rms}. $\langle u\rangle$ and u_{rms} are normalized by the mean centreline velocity $\langle u\rangle_{y0}$ and the lateral coordinate y is normalized by the jet halfwidth defined with $\langle u\rangle$. DNS results are compared with previous experiments and DNS of spatially evolving planar jets, where the legends of this figure also present the streamwise location x/H and the Reynolds number Re_J (Gutmark & Wygnanski 1976; Namer & Ötügen 1988; Deo *et al.* 2008, 2013; Terashima *et al.* 2012; Watanabe *et al.* 2014*c*; Takahashi *et al.* 2019; Matsubara *et al.* 2020; Stanley *et al.* 2002; Klein *et al.* 2003; Watanabe *et al.* 2014*b*; da Silva & Lopes 2015).

velocity fluctuations $u_{rms} = \sqrt{\langle u^2\rangle - \langle u\rangle^2}$ normalized by the mean centreline velocity $\langle u\rangle_{y0}$. The lateral position y is normalized by the jet halfwidth b_u defined with the mean streamwise velocity. The figure also includes the results of DNS and experiments of spatially evolving planar jets. Both mean velocity and rms velocity fluctuations in the present DNS agree well with previous studies, and the jet has reached a fully developed turbulent state at $t = 20t_r$. $u_{rms}/\langle u\rangle_{y0}$ has a maximum value away from the centreline. The peak value of $u_{rms}/\langle u\rangle_{y0}$ and its location y/b_u vary between 0.23-0.31 and between 0.32-0.81, respectively, among the results of the spatially evolving jet shown in figure 2(b). The peak values in the present DNS are 0.26, 0.25, 0.26 and 0.28 for $Re = 4000$, 10000, 40000 and 100000, respectively, while the peak locations for these Re_J are $y/b_u = 0.76$, 0.87, 0.78 and 0.77. The peaks and locations are within the variations among the previous studies.

Variations of u_{rms}/U_J among experiments and numerical simulations are possibly explained by the inflow conditions at the nozzle. As shown in figure 1, the Reynolds number is important in the shear layer development at the edges of the jet, and the Re dependence of the initial shear layers can affect the properties of the fully developed turbulent planar jet. In the present study, the initial shear layers have the Reynolds number $Re_\theta = U_J\theta_J/\nu$, where $\theta_J = 0.01H$ is assumed in Eq. (2.4). $Re_\theta = 0.01Re_J$ is 40 for $Re_J = 4000$ and 1000 for $Re_J = 100000$, and the viscous effects during the shear instability can be important for $Re_J = 4000$. For example, the initial velocity fluctuations decay faster at a lower Reynolds number before the transition, and the actual

fluctuations that trigger the transition can depend on Re_J (Re_θ). The mean velocity profile at the nozzle is also different among experiments and numerical simulations. Some experiments used a skimmer to eliminate the boundary layers that develop inside the nozzle. (Terashima *et al.* 2012; Takahashi *et al.* 2019) The inflow mean velocity in this case is well described by a top-hat profile (Terashima *et al.* 2018), which corresponds to (2.4) with very small θ_J. If the skimmer is not used in experiments, the inflow velocity is influenced by the boundary layers inside a nozzle (Deo *et al.* 2008; Watanabe *et al.* 2014*a*; Matsubara *et al.* 2020). Even if the jet Reynolds numbers are identical in these experiments, the Reynolds numbers of the initial shear layers are different depending on the usage of the skimmer and the shape of the nozzle. Wu *et al.* (2013) tested top-hat and parabolic profiles of the mean inflow velocity in DNS of a spatially evolving planar jet, and found that the evolution of velocity statistics is different for these profiles. The turbulent intensity defined as u_{rms}/U_J at the nozzle exit was also different among experiments and simulations. In experiments, u_{rms}/U_J at the centre of the nozzle was about 0.01 in Deo *et al.* (2008), 0.012 in Terashima *et al.* (2012) and 0.05 in Watanabe *et al.* (2014*a*) while the profile of u_{rms}/U_J inside the nozzle is very different among these experiments. It was shown that the velocity fluctuations at the nozzle exit also affect jet development (Klein *et al.* 2003). Watanabe *et al.* (2014*a*) conducted DNS of a spatially evolving planar jet with the profiles of mean velocity and rms streamwise velocity fluctuations measured in the experimental apparatus used in Watanabe *et al.* (2014*c*). The evolution of 1st- and 2nd-order statistics of velocity and passive scalar (dye concentration) was in excellent agreement between the DNS and experiment. These results indicate the importance of inflow velocity characteristics in the statistics of the fully developed turbulent jet. The rms velocity fluctuations are dominated by large-scale velocity fluctuations. DNS of a temporally evolving planar jet confirmed that the initial velocity profile affects the shape of large-scale vortices visualized by pressure isosurface (Taveira & da Silva 2013). Their DNS suggests that the initial roller vortices at the edges of the jet sometimes persist even at late time. Numerical simulations of turbulent mixing layers also found that the roller vortices of the Kelvin-Helmholtz instability can persist even in the self-similar region depending on the initial conditions, and the presence of the vortices affects the statistics in the self-similar region (Balaras *et al.* 2001). Similarly, the influence of the inflow velocity on the fully developed turbulent jet can also be related to the large-scale vortices in the jet.

The DNS databases at $t = 20t_r$ are analysed in this study. Table 1 also includes the Kolmogorov length scale $\eta = (\nu^3/\varepsilon)^{1/4}$, Taylor microscale $\lambda = \sqrt{15\nu u_0^2/\varepsilon}$, jet halfwidth b_u and turbulent Reynolds number $Re_\lambda = u_0\lambda/\nu$ at $t = 20t_r$, where $\varepsilon = 2\nu\langle S_{ij}S_{ij}\rangle$ is the mean kinetic energy dissipation rate and $u_0 = \sqrt{(u_{rms}^2 + v_{rms}^2 + w_{rms}^2)/3}$ is the characteristic velocity scale of energy-containing, large-scale motions. Here, η, λ and Re_λ are taken at the centre of the jet ($y = 0$). The spatial resolution in each direction Δ_i is compared with the Kolmogorov length scale at $y = 0$, and $\Delta_x = \Delta_z \approx 1.6\eta$ and $\Delta_y \approx 1.2\eta$ are small enough for the present central difference schemes to resolve small-scale fluctuations (Watanabe *et al.* 2018*a*).

The turbulent jet is known as an intermittent turbulent flow, where both turbulent and non-turbulent fluids appear at a given location. The turbulent fluid is separated from the non-turbulent fluid by a thin interface (da Silva *et al.* 2014). In this study, the characteristics of shear layers are compared with the length and velocity scales of turbulence. As these scales are different between turbulent and non-turbulent regions, the scales are estimated solely from the turbulent region as functions of y. The turbulent region of the planar jet can be detected with vorticity magnitude $\omega = |\boldsymbol{\omega}|$ (Bisset

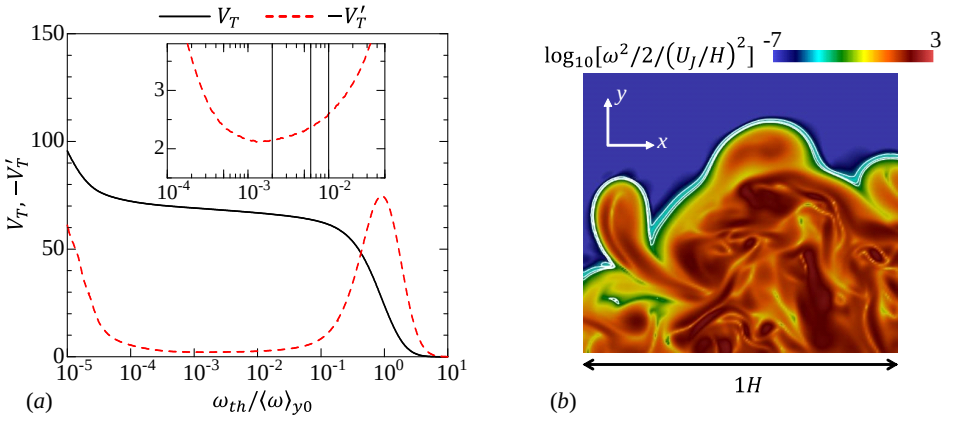

Figure 3: (a) Turbulent volume V_T and $-V_T' = -dV_T/d(\log_{10}\omega_{th})$ plotted with the detection threshold ω_{th}. The vertical lines in the inset represent ω_{th} visualized in (b). (b) Logarithmic contour of enstrophy $\omega^2/2$ and isoline of $\omega = \omega_{th}$ on a x-y plane with $\omega_{th} = 0.01\langle\omega\rangle_C$, $0.006\langle\omega\rangle_C$ and $0.002\langle\omega\rangle_{y0}$. These results are obtained in DNS for $Re = 10000$.

et al. 2002). Here, we define turbulent and non-turbulent fluids as $\omega \geqslant \omega_{th}$ and $\omega < \omega_{th}$, respectively, with a threshold ω_{th}. An appropriate value of ω_{th} is determined by ω_{th} dependence of the detected turbulent volume V_T following Taveira *et al.* (2013). Figure 3(a) shows the relation between $V_T(\omega_{th})$ and $\omega_{th}/\langle\omega\rangle_{y0}$ for $Re_J = 10000$, where $\langle\omega\rangle_{y0}$ is the mean vorticity magnitude on the jet centreline and V_T is defined as the volume normalized by H^3. As $\omega_{th}/\langle\omega\rangle_{y0}$ decreases from 10^1 to 10^{-1}, V_T increases because the turbulent fluid with large ω is detected. Then, V_T slowly varies with the threshold for $10^{-4} \lesssim \omega_{th}/\langle\omega\rangle_{y0} \lesssim 10^{-1}$. This is because the interfacial layer that separates the turbulent and non-turbulent regions occupies small volume in the flow (da Silva *et al.* 2014). Then, V_T begins to drastically increase as $\omega_{th}/\langle\omega\rangle_{y0}$ becomes smaller than 10^{-4}. The turbulent region is well detected when $\omega_{th}/\langle\omega\rangle_{y0}$ is chosen in the range where V_T weakly depends on $\omega_{th}/\langle\omega\rangle_{y0}$. This range is better appreciated by the plot of $V_T' = dV_T/d(\log_{10}\omega_{th})$, which is also shown in figure 3(a). The inset shows the range of $\omega_{th}/\langle\omega\rangle_{y0}$ with small $-V_T'$, which has a local minimum at $\omega_{th}/\langle\omega\rangle_{y0} \approx 10^{-3}$. Very small ω in the non-turbulent region often arises from errors due to numerical schemes, and is detected as a turbulent region if the threshold $\omega_{th}/\langle\omega\rangle_{y0}$ is smaller than 10^{-3}. For $\omega_{th}/\langle\omega\rangle_{y0} \gtrsim 10^{-2}$, $-V_T'$ begins to rapidly increase with ω_{th}. Therefore, the threshold can be chosen from $10^{-3} \lesssim \omega_{th}/\langle\omega\rangle_{y0} \lesssim 10^{-2}$. Figure 3($b$) shows the isolines of $\omega = \omega_{th}$ with $\omega_{th} = 0.01\langle\omega\rangle_C$, $0.006\langle\omega\rangle_C$ and $0.002\langle\omega\rangle_{y0}$ near the outer edge of the jet. The contour is the logarithmic plot of enstrophy $\omega^2/2$. Regions with large $\omega^2/2$ (shown with red colour) are considered as vortex tubes (Jiménez *et al.* 1993), whose diameter is about 10 times the Kolmogorov scale near the TNTI layer in a temporally evolving planar jet (Watanabe *et al.* 2017). The isoline location slightly changes for three thresholds. However, this change is much smaller than the size of large-enstrophy regions. In the rest of the paper, the turbulent region is detected with $\omega_{th} = 0.01\langle\omega\rangle_{y0}$. As $\langle\omega\rangle_{y0}$ varies with time and is also different depending on Re_J, the threshold is not a constant. Previous studies also used the threshold that varies with the streamwise location (time) of spatially (temporally) evolving turbulent flows (Bisset *et al.* 2002; Attili *et al.* 2014; Watanabe *et al.* 2014*b*; Zhou & Vassilicos 2017; Watanabe *et al.* 2019). If the resolution of DNS is

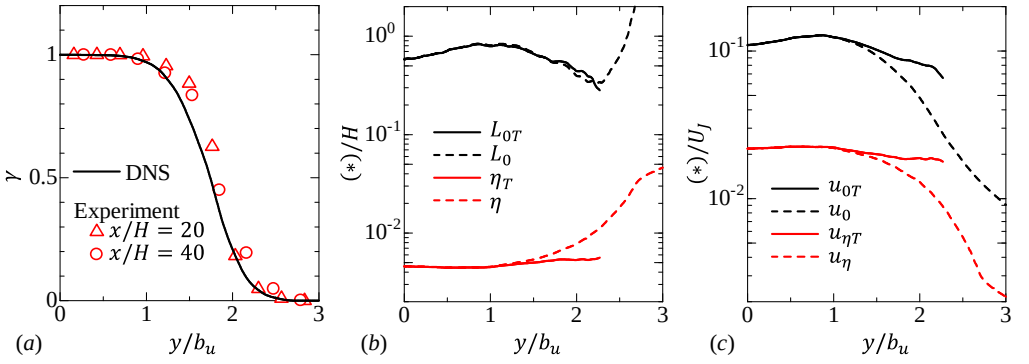

Figure 4: Lateral profiles of (a) intermittency factor γ, (b) integral length scale and Kolmogorov length scale and (c) characteristic velocity scale of large-scale motions and Kolmogorov velocity scale at $t = 20t_r$ in DNS for $Re_J = 10000$. The intermittency factor is compared with experimental data measured at the streamwise distance from the jet nozzle of $x/H = 20$ and 40 in a turbulent planar jet with $Re_J = 2200$ (Watanabe *et al.* 2015). (b) and (c) compare length and velocity scales defined with conventional averages (L_0, η, u_0 and u_η) and averages of turbulent fluids (L_{0T}, η_T, u_{0T} and $u_{\eta T}$).

not good enough, the well-defined interface is not detected with the isosurface of ω. It was shown that a low resolution causes unphysical vorticity oscillation in the concave region of the interface (concave in the view from the non-turbulent region), and the isosurface of ω becomes partially jagged (Watanabe *et al.* 2018*b*). For the present DNS code, this unphysical vorticity oscillation becomes noticeably large for $\Delta_i \gtrsim 2\eta$ (Watanabe *et al.* 2018*b*). The isoline in figure 3(b) is smooth even in the concave region, and the present DNS does not have the resolution issue on the interface detection.

We define an intermittency function $I(x, y, z)$, which is equal to 1 for $\omega(x, y, z) \geqslant \omega_{th}$ and to 0 for $\omega(x, y, z) < \omega_{th}$. An average of a variable f in the turbulent region is defined as $\langle f \rangle_T \equiv \langle If \rangle / \langle I \rangle$ (LaRue & Libby 1974), which is obtained as a function of y at each time instance. Rms velocity fluctuations in three directions are calculated as $u_{rmsT} = (\langle u^2 \rangle_T - \langle u \rangle_T^2)^{1/2}$, $v_{rmsT} = (\langle v^2 \rangle_T - \langle v \rangle_T^2)^{1/2}$ and $w_{rmsT} = (\langle w^2 \rangle_T - \langle w \rangle_T^2)^{1/2}$. The characteristic velocity and length scales of large-scale motions in the turbulent region are defined as

$$u_{0T} = \left[\frac{1}{3} (u_{rmsT}^2 + v_{rmsT}^2 + w_{rmsT}^2) \right]^{1/2}, \quad L_{0T} = \frac{u_{0T}^3}{\varepsilon_T}, \tag{2.7}$$

respectively, where $\varepsilon_T = 2\nu \langle S_{ij} S_{ij} \rangle_T$ is the kinetic energy dissipation rate averaged for the turbulent fluids. Similarly, the Kolmogorov velocity and length scales in turbulence are defined as

$$u_{\eta T} = (\nu \varepsilon_T)^{1/4}, \quad \eta_T = (\nu^3 / \varepsilon_T)^{1/4}. \tag{2.8}$$

respectively,

Figure 4(a) shows an intermittency factor $\gamma = \langle I \rangle$, which is a probability that turbulent fluid is found at y. As confirmed from $\gamma = 1$ for $y/b_u \lesssim 1$, the region near the jet centreline is always turbulent. On the other hand, γ decreases with y for $y/b_u \gtrsim 1$, where the non-turbulent region also exists intermittently. The profile of γ in the DNS agrees with experimental results of a spatially evolving planar jet. Figures 4(b, c) compare the velocity and length scales defined with conventional averages $\langle\ \rangle$ and averages of the

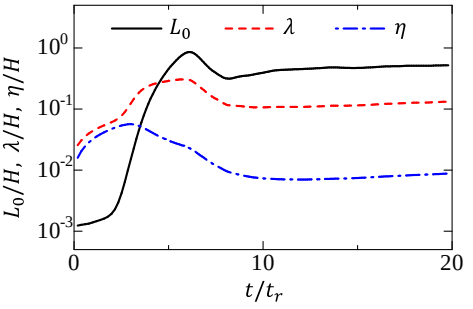

Figure 5: Temporal evolution of length scales L_0, λ and η on the jet centreline ($Re_J = 4000$).

turbulent fluids $\langle\ \rangle_T$, where the statistics calculated with $\langle\ \rangle_T$ are shown for y with $\gamma \geqslant 0.05$. Here, the integral scale is defined as $L_0 = u_0^3/\varepsilon$ (Pope 2000). In the region with $\gamma = 1$, the length and velocity scales are identical for both averages. However, these averages are different in the intermittent region with $\gamma < 1$. This is because the non-turbulent region has different characteristic length and velocity scales from the turbulent region. As the shear layers appear only in the turbulent region, the characteristics of shear layers are compared with the velocity and length scales defined with averages of the turbulent fluids. Figure 5 shows the temporal evolution of the length scales, L_0, λ and η, at $y = 0$ for $Re_J = 4000$. These length scales rapidly change with time during the turbulent transition ($t_r \lesssim 10$), and slowly increases at a later time. All results presented in this paper are taken at $t/t_r = 20$.

3. Shear layer analysis based on the triple decomposition of the velocity gradient tensor

3.1. *Triple decomposition of the velocity gradient tensor*

The triple decomposition of the velocity gradient tensor (Kolář 2007; Watanabe *et al.* 2020) is applied to the DNS databases described above. The triple decomposition decomposes the velocity gradient tensor $\nabla \boldsymbol{u}$ into three components which represent the motions of shear (S), rotation (R) and elongation (E) as $\nabla \boldsymbol{u} = \nabla \boldsymbol{u}_S + \nabla \boldsymbol{u}_R + \nabla \boldsymbol{u}_E$. In the triple decomposition, the shear tensor $\nabla \boldsymbol{u}_S$ is extracted from $\nabla \boldsymbol{u}$ as

$$(\nabla \boldsymbol{u}_S)_{ij} = \begin{cases} (\nabla \boldsymbol{u})_{ij} - \mathrm{sgn}[(\nabla \boldsymbol{u})_{ij}]\min[|(\nabla \boldsymbol{u})_{ij}|, |(\nabla \boldsymbol{u})_{ji}|] & \text{for } (i,j) = (1,2) \text{ and } (1,3) \\ 0 & \text{otherwise} \end{cases}, \tag{3.1}$$

where $\mathrm{sgn}(x)$ is the sign function. Then, $\nabla \boldsymbol{u}_E$ and $\nabla \boldsymbol{u}_R$ are obtained respectively as symmetric and anti-symmetric parts of the residual tensor $(\nabla \boldsymbol{u}_{RES})_{ij} = (\nabla \boldsymbol{u})_{ij} - (\nabla \boldsymbol{u}_S)_{ij}$:

$$(\nabla \boldsymbol{u}_E)_{ij} = [(\nabla \boldsymbol{u}_{RES})_{ij} + (\nabla \boldsymbol{u}_{RES})_{ji}]/2, \tag{3.2}$$

$$(\nabla \boldsymbol{u}_R)_{ij} = [(\nabla \boldsymbol{u}_{RES})_{ij} - (\nabla \boldsymbol{u}_{RES})_{ji}]/2. \tag{3.3}$$

Equation (3.1) ensures that $\nabla \boldsymbol{u}_S$ represents a simple shear. However, the application of (3.1) does not always extract the shearing motion of the flow. In the triple decomposition, (3.1) must be applied in a specific frame of reference where (3.1) can effectively extract the shearing motion (Kolář 2007). This reference frame is called a basic reference frame,

which is identified by a method described in appendix A. The basic reference frame assumes that the shearing motion extracted by (3.3) is the strongest in the basic reference frame among all reference frames. The decomposition applied in the basic reference frame provides $\nabla \boldsymbol{u}_S$, $\nabla \boldsymbol{u}_R$ and $\nabla \boldsymbol{u}_E$ in this frame. These tensors in the original coordinate (x, y, z) are obtained with the coordinate transformation tensor from the basic reference frame to (x, y, z) defined in appendix A.

The basic reference frame is locally determined at each grid point, where the decomposition given by (3.1)-(3.3) provides three decomposed tensors. The triple decomposition is repeatedly applied in the entire computational domain of the DNS databases to obtain the three-dimensional data of $\nabla \boldsymbol{u}_S$, $\nabla \boldsymbol{u}_R$ and $\nabla \boldsymbol{u}_E$. Intensities of shear, rotation and elongation are evaluated as $I_S = \sqrt{2(\nabla \boldsymbol{u}_S)_{ij}(\nabla \boldsymbol{u}_S)_{ij}}$, $I_R = \sqrt{2(\nabla \boldsymbol{u}_R)_{ij}(\nabla \boldsymbol{u}_R)_{ij}}$ and $I_E = \sqrt{2(\nabla \boldsymbol{u}_E)_{ij}(\nabla \boldsymbol{u}_E)_{ij}}$, respectively.

3.2. *Analysis of shear layers*

Shear layers can be detected as regions with large I_S (Eisma *et al.* 2015; Nagata *et al.* 2020). The shear layers in the planar jet are investigated with the method proposed in Watanabe *et al.* (2020), which examines the flow field around local maxima of I_S. When flow structures associated with shearing motion are identified in a three-dimensional profile of I_S, one can find at least one local maximum of I_S in the structure. Here, the local maxima can be found with a Hessian matrix of $-I_S$ defined as $H_{ij} = -\partial^2 I_S/\partial x_i \partial x_j$. We denote a variable f at an orthogonal grid point (i, j, k) by $f^{(i,j,k)}$ and the spatial derivative of f by $\partial_{x_i} f = \partial f/\partial x_i$, where (i, j, k) represents the location of grid points in x, y and z directions. Local maxima of I_S used for the analysis of the shear layers are identified as grid points (i, j, k) that satisfy the following conditions:

$$(\partial_x I_S)^{(i-1,j,k)}(\partial_x I_S)^{(i+1,j,k)} < 0, \tag{3.4}$$

$$(\partial_y I_S)^{(i,j-1,k)}(\partial_y I_S)^{(i,j+1,k)} < 0, \tag{3.5}$$

$$(\partial_z I_S)^{(i,j,k-1)}(\partial_z I_S)^{(i,j,k+1)} < 0, \tag{3.6}$$

$$H_{11}^{(i,j,k)} > 0, \quad (H_{11}H_{22} - H_{12}H_{21})^{(i,j,k)} > 0, \tag{3.7}$$

$$(H_{11}H_{22}H_{33} + H_{12}H_{23}H_{31} + H_{13}H_{21}H_{32} - H_{13}H_{22}H_{31} - H_{11}H_{23}H_{32} - H_{12}H_{21}H_{33})^{(i,j,k)} > 0, \tag{3.8}$$

$$\mathrm{sgn}[(\partial_x I_S)^{(i-1,j,k)}] = \mathrm{sgn}[(\partial_x I_S)^{(i-2,j,k)}] = \mathrm{sgn}[(\partial_x I_S)^{(i-3,j,k)}], \tag{3.9}$$

$$\mathrm{sgn}[(\partial_y I_S)^{(i,j-1,k)}] = \mathrm{sgn}[(\partial_y I_S)^{(i,j-2,k)}] = \mathrm{sgn}[(\partial_y I_S)^{(i,j-3,k)}], \tag{3.10}$$

$$\mathrm{sgn}[(\partial_z I_S)^{(i,j,k-1)}] = \mathrm{sgn}[(\partial_z I_S)^{(i,j,k-2)}] = \mathrm{sgn}[(\partial_z I_S)^{(i,j,k-3)}], \tag{3.11}$$

$$\mathrm{sgn}[(\partial_x I_S)^{(i+1,j,k)}] = \mathrm{sgn}[(\partial_x I_S)^{(i+2,j,k)}] = \mathrm{sgn}[(\partial_x I_S)^{(i+3,j,k)}], \tag{3.12}$$

$$\mathrm{sgn}[(\partial_y I_S)^{(i,j+1,k)}] = \mathrm{sgn}[(\partial_y I_S)^{(i,j+2,k)}] = \mathrm{sgn}[(\partial_y I_S)^{(i,j+3,k)}], \tag{3.13}$$

$$\mathrm{sgn}[(\partial_z I_S)^{(i,j,k+1)}] = \mathrm{sgn}[(\partial_z I_S)^{(i,j,k+2)}] = \mathrm{sgn}[(\partial_z I_S)^{(i,j,k+3)}]. \tag{3.14}$$

Equations (3.4)-(3.8) ensure that I_S attains a local maximum at (i, j, k). Local maxima of I_S can also appear in noise-like patterns of very small I_S, which are not related to the shear layer structures of turbulence. These points can be eliminated from the analysis with additional conditions (3.9)-(3.14). It was shown that these criteria successfully identify shear layers in isotropic turbulence in Watanabe *et al.* (2020). Values of I_S are different depending on flows and Reynolds numbers. However, the detection criterion given by (3.4)-(3.14) uses the sign of the gradient of I_S and the location of the local

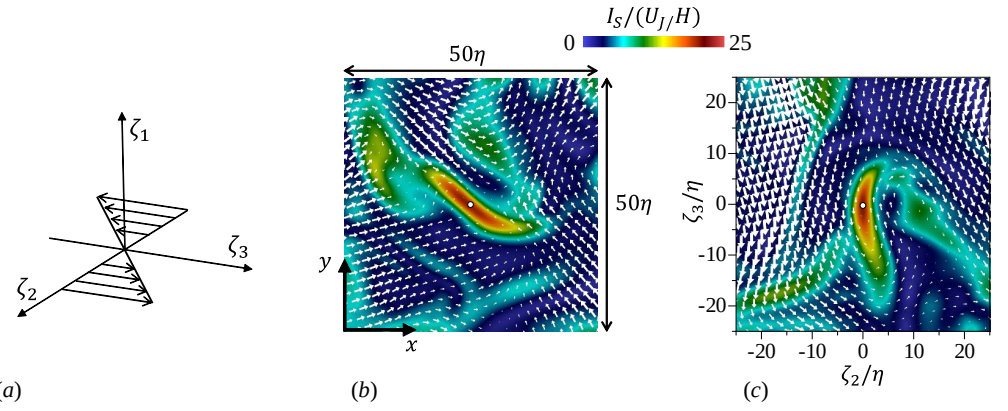

Figure 6: (a) Shear coordinate defined with a shear tensor $\nabla \boldsymbol{u}_S$. A flow field around a local maximum of I_S used in the shear layer analysis: (b) x-y plane; (c) ζ_2-ζ_3 plane of the shear coordinate. A circle at the centre of the figures marks the location of the local maximum of I_S. The relative velocity with respect to the local maximum location of I_S is shown on each plane.

maxima of I_S, and does not rely on the value of I_S itself. Therefore, (3.4)-(3.14) are expected to be useful in the shear layer detection in various turbulent flows.

We introduce a shear coordinate system $(\zeta_1, \zeta_2, \zeta_3)$ for each point of local maxima of I_S that satisfies (3.4)-(3.14). The orientations of ζ_1, ζ_2 and ζ_3 are represented by unit vectors $\boldsymbol{n}_1$, $\boldsymbol{n}_2$ and $\boldsymbol{n}_3$, respectively. In the Cartesian coordinate used in the DNS, the unit vector $\boldsymbol{n}_i$ is expressed with three components as $((\boldsymbol{n}_i)_x, (\boldsymbol{n}_i)_y, (\boldsymbol{n}_i)_z)$. The shear coordinate assumes that the shear is expressed with the derivative of $\boldsymbol{n}_3$-directional velocity with respect to ζ_2 as illustrated in figure 6(a). The shear coordinate is identified with the method used in Watanabe *et al.* (2020). First, $\boldsymbol{n}_1$ is determined as the direction of the vorticity vector of the shear tensor, $\boldsymbol{n}_1 = \boldsymbol{\omega}_S/|\boldsymbol{\omega}_S|$, with $(\boldsymbol{\omega}_S)_i = \epsilon_{ijk}(\nabla \boldsymbol{u}_S)_{jk}$, where ϵ_{ijk} is the Levi-Civita symbol. Then, $\boldsymbol{n}_2$ and $\boldsymbol{n}_3$ are determined so that the shear tensor $\nabla \boldsymbol{u}_S$ satisfies the following relation in the shear coordinate:

$$(\nabla \boldsymbol{u}_S)_{ij} \neq 0 \quad \text{for } (i,j) = (3,2), \tag{3.15}$$

$$(\nabla \boldsymbol{u}_S)_{ij} = 0 \quad \text{otherwise.} \tag{3.16}$$

$\boldsymbol{n}_2$ and $\boldsymbol{n}_3$ are obtained with the method presented in appendix B.

Once the shear coordinate is identified for each local maximum of I_S, flow variables on $(\zeta_1, \zeta_2, \zeta_3)$ are interpolated from the DNS grid by using a third-order Lagrange polynomial interpolation scheme. The relative velocity with respect to $(\zeta_1, \zeta_2, \zeta_3) = (0, 0, 0)$ is used in the present analysis, where ζ_1, ζ_2 and ζ_3 components of the relative velocity are denoted by u_1, u_2 and u_3, respectively. Figures 6(b, c) show a flow field around a local maximum of I_S at $y = 0$ of the jet with $Re_J = 10000$. The shear layer is visualized as a thin region with large I_S. The velocity vector on the x-y plane does not show the shear layer pattern. However, after the coordinate transformation from (x, y, z) to $(\zeta_1, \zeta_2, \zeta_3)$, the shear is well represented by the velocity in $\pm\zeta_3$ directions for $\zeta_2 > 0$ and $\zeta_2 < 0$ in figure 6(c). The coordinate transformaton from (x, y, z) to $(\zeta_1, \zeta_2, \zeta_3)$ is applied at all local maxima of I_S that satisfy (3.4)-(3.14). Ensemble averages of the interpolated variables are taken as functions of $(\zeta_1, \zeta_2, \zeta_3)$ with a large number of detected local maxima of I_S. This average is denoted by $\overline{f}$. Statistics in the temporally evolving turbulent planar jet depend on y and

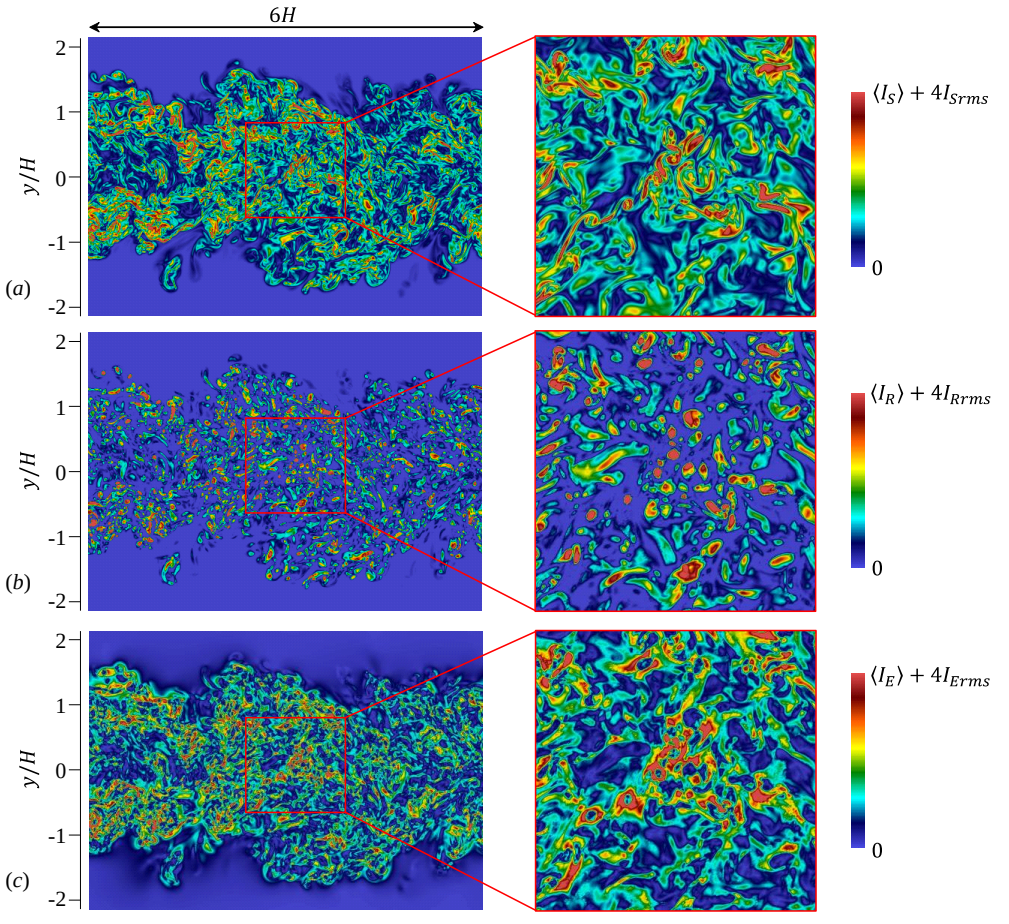

Figure 7: Colour contour plots of (a) I_S, (b) I_R and (c) I_E on a x-y plane in the planar jet with $Re_J = 10000$ ($t = 20t_r$). The maximum value of colour contour $\langle I_\alpha \rangle + 4I_{\alpha rms}$ ($\alpha = S, R$ or E) is determined with the statistics at $y = 0$.

time. Therefore, the ensemble averages at a given time step are also taken as functions of y, i.e. $\overline{f}(y; \zeta_1, \zeta_2, \zeta_3)$. As presented below, shearing motion hardly exists outside the jet, and the number of samples of the shear layers becomes very small near the outer edge of the jet. Therefore, the analysis of shear layers is conducted for $0 \leqslant y \leqslant 2b_u$ because the turbulent fluid hardly appears beyond $y = 2b_u$. Detected local maxima of I_S are binned into 11 bins centred at $y/b_u = 0, 0.2, 0.4, ...,$ and 2.0, where all bins have equal width of $0.2b_u$. The ensemble averages are taken with all local maxima of I_S in each bin. For example, a local maximum of I_S found at $y = 0.25b_u$ is used as a sample of the statistics calculated at $y/b_u = 0.2$.

4. Results and Discussion

4.1. *Flow visualization with tensors obtained by the triple decomposition*

Figure 7 visualizes I_S, I_R and I_E on a x-y plane of the planar jet with $Re_J = 10000$. The intensities of three motions tend to be large inside the jet. In figure 7(a), large I_S

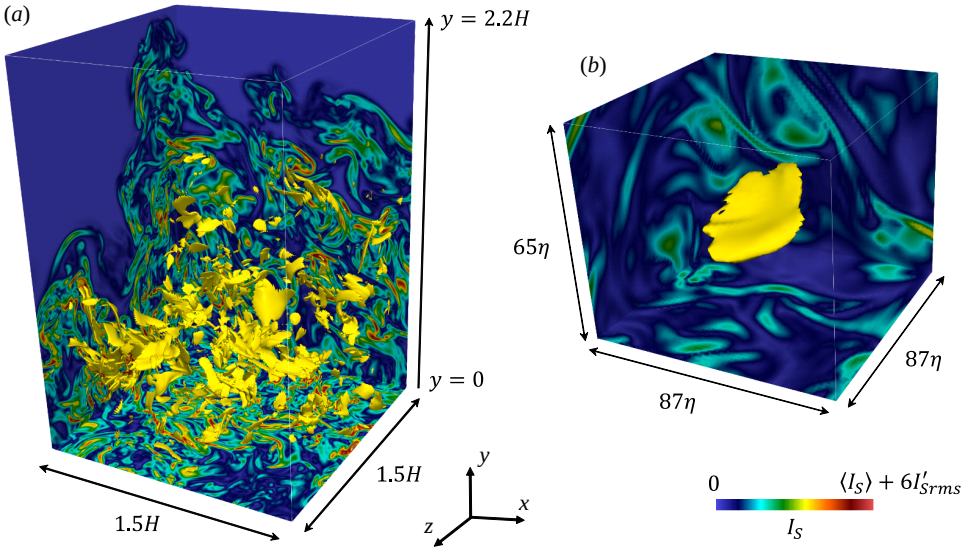

Figure 8: (a) Visualization of isosurfaces of $I_S = I_{Sth}$ in the planer jet with $Re_J = 10000$ ($t = 20t_r$), where $I_{Sth} = \langle I_S \rangle + 4I_{Srms}$ is calculated with $\langle I_S \rangle$ and I_{Srms} at $y = 0$. (b) Close-up of one of the isosurfaces in (a).

often appears as a thin line. On the other hand, large I_R often has a circular shape in figure 7(b). These patterns of large I_S and I_R are two-dimensional cuts of sheetlike and tubular structures of intense shear and rotation, respectively. Comparison of figures 7(b) and (c) indicates that I_E tends to be large around circular regions with large I_R. These distributions of I_S, I_R and I_E in the planar jet are consistent with DNS results of homogeneous isotropic turbulence (Nagata *et al.* 2020).

Figure 8 visualizes isosurfaces of $I_S = \langle I_S \rangle + 4I_{Srms}$ in the planar jet with $Re_J = 10000$, where the isosurface value is determined by $\langle I_S \rangle$ and I_{Srms} at $y = 0$. A large number of thin sheetlike structures are visualized with I_S, which detects well the shear layers in the turbulent planar jet. Similar structures were also identified with I_S in homogeneous isotropic turbulence (Watanabe *et al.* 2020). The flow field around the shear layers is investigated with the averages taken in the shear coordinate in § 4.3.

4.2. *Statistics of tensors of shear, rotation and elongation*

Figure 9 shows the lateral profiles of averages of the intensities of three motions, $\langle I_S \rangle$, $\langle I_R \rangle$ and $\langle I_E \rangle$ in the planar jet with $Re_J = 10000$. The averaged intensities weakly depend on y for $|y/b_u| \lesssim 0.8$, and decreases with $|y|$ for $|y/b_u| \gtrsim 0.8$ because the flow outside the jet has small velocity gradients. For $|y/b_u| \lesssim 2$, $\langle I_S \rangle$ is the largest among three motions, and the turbulent jet is dominated by shearing motion. The intermittency factor in figure 4(a) indicates that the turbulent region of the jet hardly reaches $|y/b_u| \gtrsim 2.5$, where $\langle I_E \rangle$ is larger than $\langle I_S \rangle$ and $\langle I_R \rangle$. It is known that the velocity gradient is not negligible outside a turbulent jet because of velocity fluctuations induced by the jet (da Silva & Pereira 2008). Figure 9 further confirms that the induced velocity fluctuations are associated with elongation $\nabla \boldsymbol{u}_E$ rather than rotation and shear, which seem to be important only inside the turbulent jet region.

The enstrophy production $P_\omega = \omega_i S_{ij} \omega_j$ can be decomposed with the triple decompo-

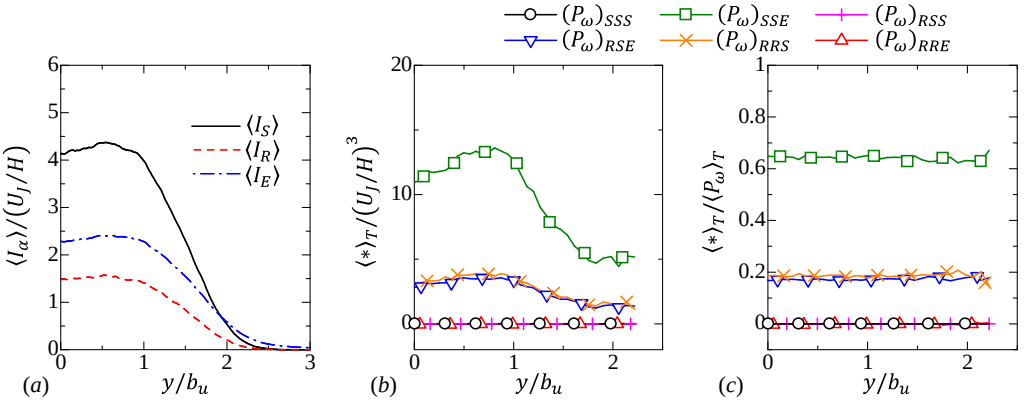

Figure 9: (a) Lateral profiles of mean values of I_S, I_R and I_E. (b) Averages of enstrophy production terms in (4.1). (c) Relative contribution to mean enstrophy production $\langle(P_\omega)_{\alpha\beta\gamma}\rangle_T/\langle P_\omega\rangle_T$. The results are taken from the planar jet with $Re_J = 10000$ ($t = 20t_r$).

sition as (Watanabe *et al.* 2020)

$$P_\omega = (P_\omega)_{SSS} + (P_\omega)_{SSE} + (P_\omega)_{RSS} + (P_\omega)_{RSE} + (P_\omega)_{RRS} + (P_\omega)_{RRE}, \tag{4.1}$$

with

$$(P_\omega)_{SSS} = (\boldsymbol{\omega}_S)_i(\boldsymbol{\omega}_S)_j(S_S)_{ij};\ (P_\omega)_{SSE} = (\boldsymbol{\omega}_S)_i(\boldsymbol{\omega}_S)_j(\nabla\boldsymbol{u}_E)_{ij};$$
$$(P_\omega)_{RSS} = 2(\boldsymbol{\omega}_R)_i(\boldsymbol{\omega}_S)_j(S_S)_{ij};\ (P_\omega)_{RSE} = 2(\boldsymbol{\omega}_R)_i(\boldsymbol{\omega}_S)_j(\nabla\boldsymbol{u}_E)_{ij};$$
$$(P_\omega)_{RRS} = (\boldsymbol{\omega}_R)_i(\boldsymbol{\omega}_R)_j(S_S)_{ij};\ (P_\omega)_{RRE} = (\boldsymbol{\omega}_R)_i(\boldsymbol{\omega}_R)_j(\nabla\boldsymbol{u}_E)_{ij}.$$

Here, $(S_S)_{ij} = [(\nabla\boldsymbol{u}_S)_{ij} + (\nabla\boldsymbol{u}_S)_{ji}]/2$ is a symmetric part of the shear tensor and $(\boldsymbol{\omega}_S)_i = \epsilon_{ijk}(\nabla\boldsymbol{u}_S)_{jk}$ and $(\boldsymbol{\omega}_R)_i = \epsilon_{ijk}(\nabla\boldsymbol{u}_R)_{jk}$ are the vorticity vectors of $\nabla\boldsymbol{u}_S$ and $\nabla\boldsymbol{u}_R$, respectively. The decomposed terms represent the interactions of three motions considered in the triple decomposition. Figure 9(b) shows the averages of these decomposed terms, where the averages are taken in the turbulent region as $\langle(P_\omega)_{\alpha\beta\gamma}\rangle_T$. The interaction between motions of shear and elongation, $\langle(P_\omega)_{SSE}\rangle_T$, has a dominant contribution to the mean enstrophy production while $\langle(P_\omega)_{RSE}\rangle_T$ and $\langle(P_\omega)_{RRS}\rangle_T$ also have positive values. These terms involve the interactions of shearing motion with other motions. The enstrophy production is large near the centreline and decreases in the intermittent region ($y/b_u \gtrsim 1$). The relative contributions to the mean enstrophy production are evaluated by $\langle(P_\omega)_{\alpha\beta\gamma}\rangle_T/\langle P_\omega\rangle_T$. In the turbulent planar jet, $\langle(P_\omega)_{SSE}\rangle_T/\langle P_\omega\rangle_T \approx 0.65$, $\langle(P_\omega)_{RSE}\rangle_T/\langle P_\omega\rangle_T \approx 0.17$ and $\langle(P_\omega)_{RRS}\rangle_T/\langle P_\omega\rangle_T \approx 0.19$ hardly vary in the y direction. In homogeneous isotropic turbulence, $\langle(P_\omega)_{SSE}\rangle/\langle P_\omega\rangle \approx 0.69$, $\langle(P_\omega)_{RSE}\rangle/\langle P_\omega\rangle \approx 0.17$ and $\langle(P_\omega)_{RRS}\rangle/\langle P_\omega\rangle \approx 0.18$ were obtained for $Re_\lambda = 43$-296 (Watanabe *et al.* 2020). Thus, the relative contributions of the decomposed production terms are similar for the planar jet and homogeneous isotropic turbulence, and the physical mechanism of the enstrophy production is the same for these flows.

Figures 10(a,b) show probability density functions (PDF) of I_S, I_R and I_E at $y = 0$ and $1.2b_u$ in the planar jet with $Re_J = 10000$. Figure 10(c) shows the PDF obtained with the DNS database of statistically stationary, homogeneous isotropic turbulence with $Re_\lambda = 72$ (Watanabe *et al.* 2020). The turbulent jet at $y = 0$ and isotropic turbulence have similar PDF of I_S, I_R and I_E. The PDF of I_R has a large peak at $I_R = 0$, and

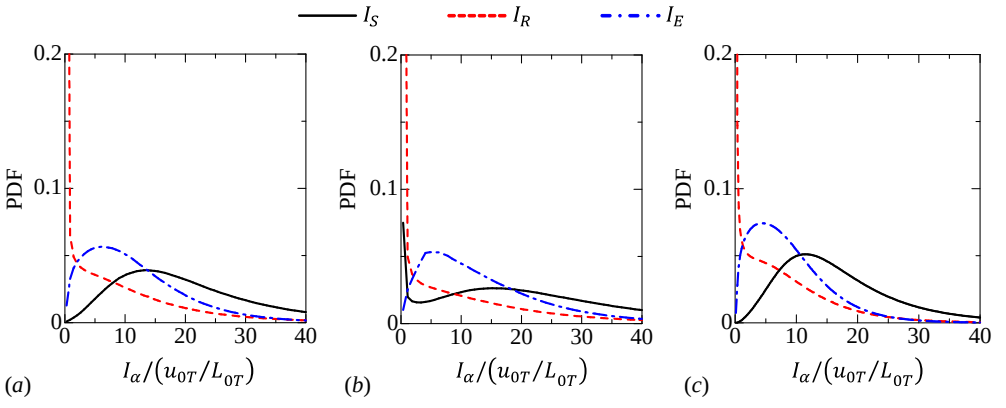

Figure 10: Probability density functions (PDF) of I_S, I_R and I_E at (a) $y = 0$ and (b) $y = 1.2b_u$ of the planar jet with $Re_J = 10000$ ($t = 20t_r$). (c) PDF of I_S, I_R and I_E in homogeneous isotropic turbulence with $Re_\lambda = 72$ taken from DNS used in Watanabe *et al.* (2020).

the motion of rotation is mostly negligible and appears intermittently in space. This is also confirmed in figure 7(b), where regions with $I_R > 0$ occupy a small part of the flow. On the other hand, the PDF of I_S and I_E has a peak for $I_S > 0$ and $I_E > 0$, and the turbulent jet has moderately strong motions of shear and elongation in most part of the flow. In figure 10(b), the PDF at $y = 1.2b_u$ has a peak at $I_S = 0$. Turbulent and non-turbulent regions intermittently exist at this location. Therefore, the peak of PDF at $I_S = 0$ is caused by the existence of non-turbulent fluid where shearing motion is absent. However, the PDF at $I_E = 0$ is still low even at $y = 1.2b_u$, indicating that the non-turbulent fluid near the jet also has moderately strong motion of elongation. For the same reason, $\langle I_E \rangle$ decreases more slowly with large y than $\langle I_S \rangle$ in figure 9.

4.3. *Mean flow characteristics around shear layers*

Mean flow patterns around the shear layers are studied with ensemble averages taken for local maxima of I_S with (3.9)-(3.14). Figure 11 shows two-dimensional profiles of the mean velocity vector $(\overline{u_1}, \overline{u_2}, \overline{u_3})$ and a colour contour of the mean shear intensity $\overline{I_S}$ obtained at $y = 0$. Here, figures 11(a) and (b) visualize the ζ_2-ζ_3 plane at $\zeta_1 = 0$ and the ζ_1-ζ_2 plane at $\zeta_3 = 0$, respectively. A region with large $\overline{I_S}$ has a flattened shape, which is expanded in the ζ_1 and ζ_3 directions. The thickness of the region with large $\overline{I_S}$ is about $5\eta_T$ in the ζ_2 direction while its spatial extent in the ζ_1 and ζ_3 directions is about $20\eta_T$. A shear layer pattern due to the flows in $\pm\zeta_3$ directions can be observed in the velocity vector on the ζ_2-ζ_3 plane in figure 11(a). The mean velocity vector in figure 11(b) exhibits biaxial strain with compression in the ζ_2 direction and stretching in the ζ_1 direction. The ζ_1 direction is taken in the direction of the vorticity of shear $\boldsymbol{\omega}_S$, which is effectively amplified by the stretching in the ζ_1 direction. This observation is consistent with figures 9(b, c), where the enstrophy production is dominated by the interaction between motions of shear and elongation. The shear layers in homogeneous isotropic turbulence also cause the enstrophy production by this interaction (Watanabe *et al.* 2020). Figure 12 presents the results obtained at $y/b_u = 1$, where the mean velocity gradient is large as shown in figure 2(a). The mean velocity vector and the profile of I_S are similar at $y/b_u = 0$ and 1. Similar mean flow patterns of the shear and biaxial strain were found for the shear layers in homogeneous isotropic turbulence (Watanabe *et al.*

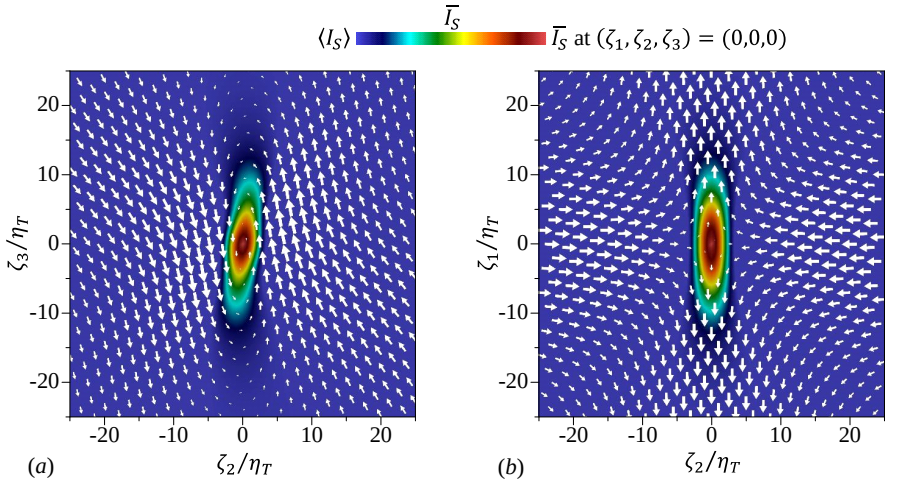

Figure 11: Mean velocity vector and colour contour of $\overline{I_S}$ on (a) ζ_2-ζ_3 plane at $\zeta_1 = 0$ and (b) ζ_1-ζ_2 plane at $\zeta_3 = 0$. The length of the vectors represents the magnitude of the velocity vector on each plane. The results are taken at $y = 0$ of the planar jet with $Re_J = 10000$.

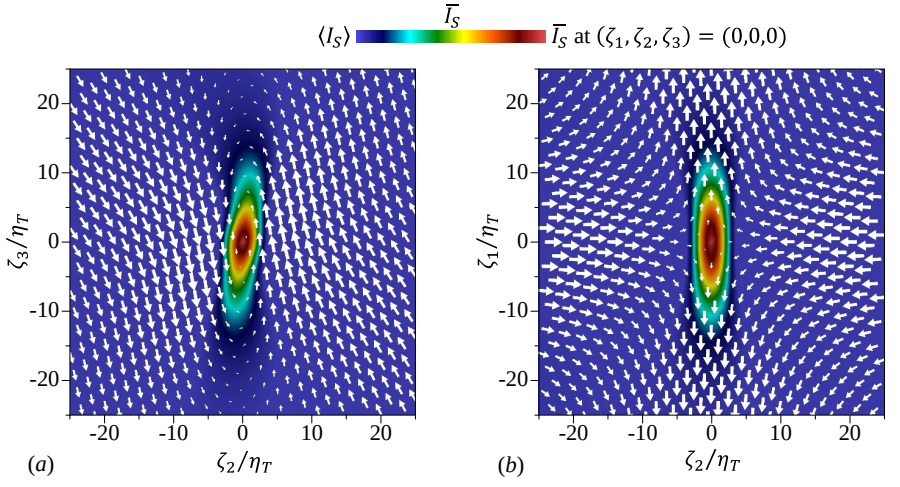

Figure 12: Mean velocity vector and $\overline{I_S}$ of the shear layers at $y/b_u = 1$ ($Re_J = 10000$). (a) ζ_2-ζ_3 plane at $\zeta_1 = 0$ and (b) ζ_1-ζ_2 plane at $\zeta_3 = 0$.

2020). Thus, the local flow topology associated with shearing motion is not qualitatively influenced by the mean velocity gradient of the planar jet.

Figure 13 shows the mean velocity profile along the ζ_1 and ζ_2 axes, where $\overline{u_1}$ on the ζ_1 axis and $\overline{u_2}$ and $\overline{u_3}$ on the ζ_2 axis significantly change near the centre of the shear layer. These velocity components are associated with the shear and biaxial strain and have large positive and negative peaks. The shear layer formed in the region of biaxial strain is consistent with Burgers' vortex layer, which is one of the exact solutions of Navier-Stokes equations (Davidson 2004). Burgers' vortex layer has a velocity profile

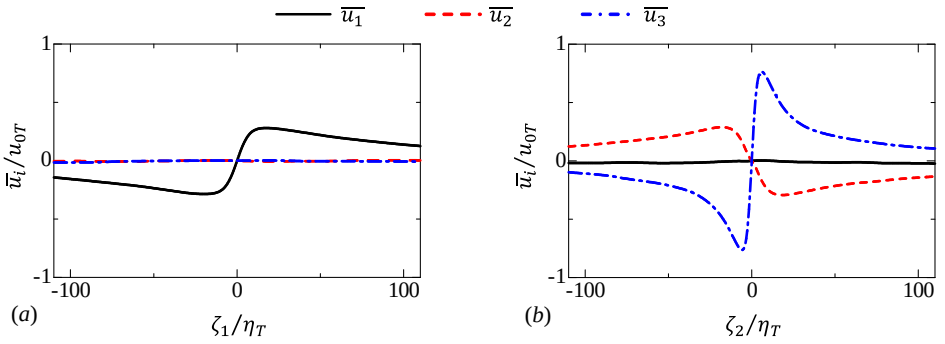

Figure 13: Mean velocity profiles around local maxima of I_S on (a) ζ_1 axis and (b) ζ_2 axis. The results are taken on the centreline of the planar jet with $Re_J = 10000$.

given by

$$u_1 = \alpha\zeta_1, \quad u_2 = -\alpha\zeta_2, \quad u_3 = \Delta u_3 \mathrm{erf}(\zeta_2/\delta), \tag{4.2}$$

where δ is the thickness of the layer and Δu_3 is the velocity jump, which is related to the shear intensity by $I_S = \sqrt{2(\partial u_3/\partial\zeta_2)^2}$. A parameter α represents the intensity of the biaxial strain acting on Burgers' vortex layer, where I_E of the triple decomposition is related to α by $\alpha = I_E/2$. The velocity profile around $(\zeta_1, \zeta_2, \zeta_3) = (0, 0, 0)$ in the planar jet is consistent with Burgers' vortex layer as confirmed from $\partial u_1/\partial\zeta_1 > 0$, $\partial u_2/\partial\zeta_2 < 0$ and $\partial u_3/\partial\zeta_2 > 0$ at $(\zeta_1, \zeta_2, \zeta_3) = (0, 0, 0)$ in figure 13. In a steady state, the thickness δ of Burgers' vortex layer is determined by α and ν as $\delta = \sqrt{2\nu/\alpha}$. If the biaxial strain were absent, the layer thickness would grow with time because of viscous diffusion (Davidson 2004). Therefore, compression due to the biaxial strain keeps the shear layer thin in Burgers' vortex layer. Figure 11 suggests that the thinning effect by the biaxial strain also exists for the shear layers in the planar jet, where the compression in the ζ_2 direction is caused by the biaxial strain. One of the apparent differences between the shear layers in the planar jet and Burgers' vortex layer is the spatial extent in the ζ_1 and ζ_3 directions. The region with large $\overline{I_S}$ appears for $|\zeta_1| \lesssim 10\eta_T$ and $|\zeta_3| \lesssim 10\eta_T$ in figure 11 while Burgers' vortex layer has an infinite length in the ζ_1 and ζ_3 directions. Visualization of the shear layers in figure 8(b) also suggests that the size of the shear layer in these directions is of the order of 10 times the Kolmogorov length scale.

4.4. *Reynolds number dependence of shear layers*

The mean velocity jump around the centre of the shear layer is found for $\overline{u_1}$ on the ζ_1 axis and $\overline{u_2}$ and $\overline{u_3}$ on the ζ_2 axis in figure 13. The velocity jump Δu_i is quantified with local maximum and minimum of these mean velocity components as shown in figure 14, where an example of $\overline{u_i}$ is shown on ζ_α axis. The width δ_i of the velocity jump Δu_i is estimated with the mean velocity gradient in the shear layer $\partial\overline{u_i}/\partial\zeta_\alpha$ as $\delta_i = \Delta u_i/|\partial\overline{u_i}/\partial\zeta_\alpha|$, where $\alpha = 1$ for $\overline{u_1}$ and $\alpha = 2$ for $\overline{u_2}$ and $\overline{u_3}$ are considered. δ_i is defined for the small-scale shear layers, where local shear arises from velocity fluctuations, and this length is expected to be smaller than the length scale that characterizes the mean shear (Thiesset *et al.* 2014). Reynolds number dependence of Δu_i and δ_i on the jet centreline is examined in this subsection in comparison with DNS results of homogeneous isotropic turbulence (Watanabe *et al.* 2020). The dependence on the lateral position in the planar jet is addressed in the next subsection.

Figure 15 shows the mean velocity jumps Δu_i normalized by the Kolmogorov velocity

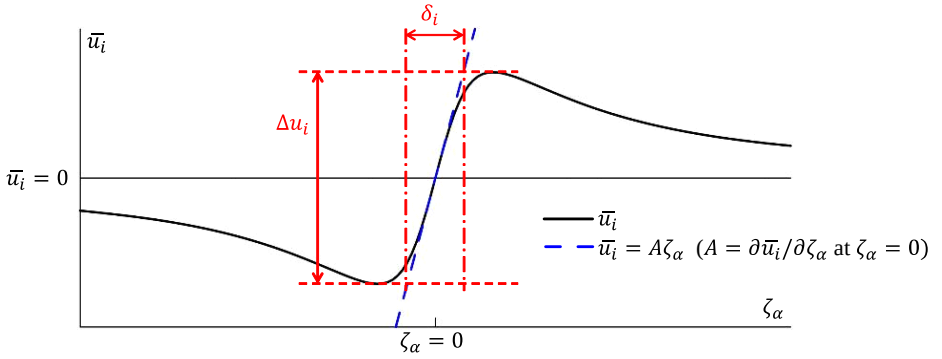

Figure 14: Definitions of the velocity jump Δu_i and its width δ_i of a mean velocity profile around shear layers.

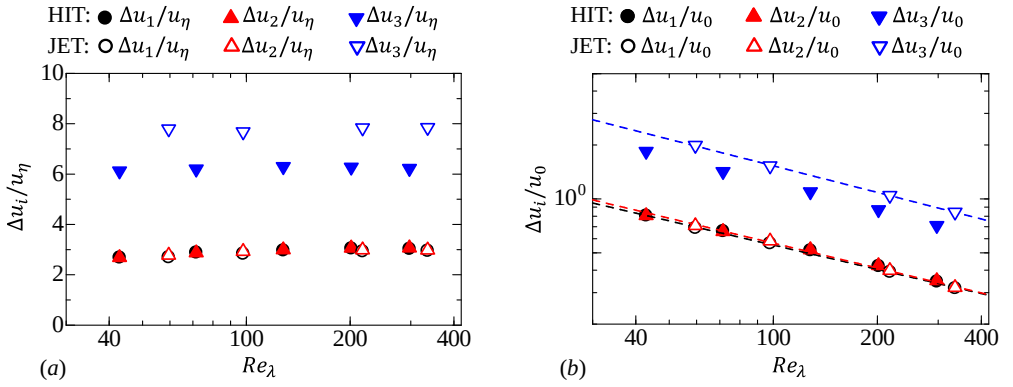

Figure 15: Re_λ dependence of the mean velocity jumps around shear layers: (a) Δu_i normalized by the Kolmogorov velocity scale u_η; (b) Δu_i normalized by the velocity scale of large-scale motions u_0. The results at the centre $(y = 0)$ of the planar jets (JET) are compared with DNS results of homogeneous isotropic turbulence (HIT) (Watanabe *et al.* 2020). The broken lines in (b) represent power laws obtained with a least square method applied to the jet data.

scale u_η or the characteristic velocity scale of large-scale motions, u_0, as functions of the turbulent Reynolds number Re_λ. $\Delta u_i/u_\eta$ hardly depends on Re_λ while $\Delta u_i/u_0$ decreases with Re_λ. Both homogeneous isotropic turbulence and planer jet have $\Delta u_1/u_\eta \approx \Delta u_2/u_\eta \approx 3$. These velocity components are associated the biaxial strain acting on the shear layer. $\Delta u_3/u_\eta$ is slightly larger in the planar jet than in the homogeneous isotropic turbulence although this difference is small: $\Delta u_3/u_\eta \approx 7.8$ in the jet and $\Delta u_3/u_\eta \approx 6.2$ in the homogeneous isotropic turbulence. Therefore, the velocity jumps around the shear layers scale with the Kolmogorov velocity scale in the planar jet and homogeneous isotropic turbulence. The broken lines in figure 15(b) represent a power law $\Delta u_i/u_0 \sim Re_\lambda^{a_i}$ with the exponent a_i obtained with a least square method applied for the data of the planar jet. The ratio between u_0 and u_η varies with a power law of Re_λ as $u_\eta/u_0 \sim Re_\lambda^{-0.5}$ in isotropic turbulence (Pope 2000), and constant $\Delta u_i/u_\eta$ implies $\Delta u_i/u_0 \sim Re_\lambda^{-0.5}$. The present DNS data of the planar jet yields $a_1 = -0.45$, $a_2 = -0.46$ and $a_3 = -0.49$, which are close to the exponent -0.5 predicted from constant $\Delta u_i/u_\eta$.

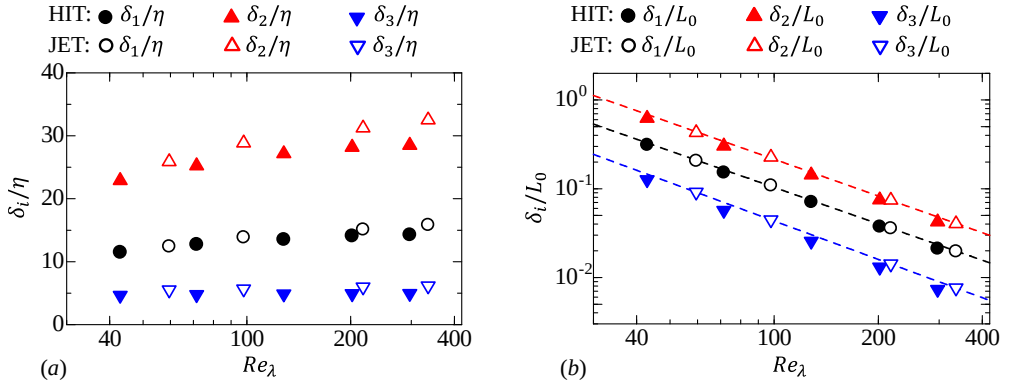

Figure 16: Re_λ dependence of the characteristic length scales δ_i of shear layers: (a) δ_i normalized by the Kolmogorov length scale η; (b) δ_i normalized by the integral scale L_0. The results at the centre ($y = 0$) of the planar jets (JET) are compared with DNS results of homogeneous isotropic turbulence (HIT) (Watanabe *et al.* 2020). The broken lines in (b) represent power laws obtained with a least square method applied to the jet data.

However, a_1 and a_2 are slightly smaller than -0.5, and $\Delta u_2/u_\eta$ and $\Delta u_3/u_\eta$ gradually increase with Re_λ.

Figure 16 compares Re_λ dependence of δ_i between the planar jet and homogeneous isotropic turbulence, where δ_i is normalized by the Kolmogorov length scale η in figure 16(a) and the integral scale L_0 in figure 16(b). In both figures, difference between the planar jet and homogeneous isotropic turbulence is small, and the normalized length scales of the shear layer hardly depend on the flows. As also found for Δu_3, δ_3/η hardly varies with the Reynolds number. In the planar jet, $\delta_3/\eta = 6$ is obtained by averaging the results of all Reynolds numbers examined in this study. On the other hand, δ_1/η and δ_2/η increase with Re_λ. However, Re_λ dependence is much smaller for δ_1/η and δ_2/η than for δ_1/L_0 and δ_2/L_0. As η/L_0 varies with $Re_\lambda^{-1.5}$ in isotropic turbulence (Pope 2000), we expect a power law of $\delta_i/L_0 \sim Re_\lambda^{-1.5}$ when δ_i/η is constant. Figure 16(b) shows δ_i/L_0 with a power law $\delta_i/L_0 \sim Re_\lambda^{b_i}$ obtained with a least square method applied to the jet data. The present DNS results yield $b_1 = -1.36$, $b_2 = -1.37$ and $b_3 = -1.44$, which are close to -1.5 expected from constant δ_i/η. Therefore, the shear layers are small-scale structures whose length scales are characterized by the Kolmogorov length scale.

If Δu_i scales with the velocity scale defined with the Taylor microscale, ν/λ (Cafiero & Vassilicos 2020), Δu_i follows $\Delta u_i/u_0 \sim Re_\lambda^{-1}$. The present DNS yields $\Delta u_i/u_0 \sim Re_\lambda^{a_i}$ with $a_1 = -0.45$, $a_2 = -0.46$ and $a_3 = -0.49$, which are closer to the exponent of the the Kolmogorov scaling -0.5 than -1. The scaling for δ_i with the Taylor microscale requires $\delta_i/L_0 \sim Re_\lambda^{-1}$ while figure 16 yields $\delta_i/L_0 \sim Re_\lambda^{b_i}$ with $b_1 = -1.36$, $b_2 = -1.37$ and $b_3 = -1.44$. These exponents are also closer to that of the Kolmogorov scaling -1.5 than -1. Thus, the length and velocity of the shear layers better scale with the Kolmogorov scale than the Taylor microscale. The differences of b_i from -1.5 are slightly larger for $i = 1$ and 2 than 3. Therefore, δ_1/η and δ_2/η increase with Re_λ in figure 16(a) and the size of the shear layers in these directions is not determined solely by η. This tendency is observed in both planar jet and homogeneous isotropic turbulence.

Figure 17 shows the number density N_{SH} of local maxima of I_S used in the shear layer analysis. N_{SH} is calculated as the number of the local maxima of I_S divided by the volume of the turbulent region V_T. If the turbulent region is filled by the shear

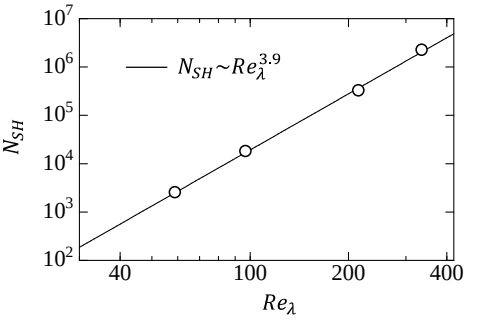

Figure 17: The number density N_{SH} of local maxima of I_S used in the shear layer analysis. N_{SH} calculated in the entire turbulent region of the jet is plotted against Re_λ on the jet centreline.

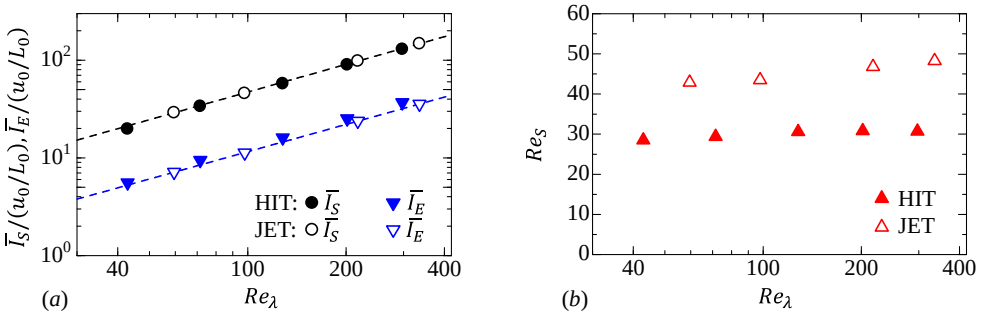

Figure 18: Re_λ dependence of (a) mean intensities of shear $\overline{I_S}$ and elongation $\overline{I_E}$ at $(\zeta_1, \zeta_2, \zeta_3) = (0, 0, 0)$ normalized by u_0/L_0 and (b) shear Reynolds number Re_S. The results at the centre $(y = 0)$ of the planar jets (JET) are compared with DNS results of homogeneous isotropic turbulence (HIT) (Watanabe *et al.* 2020). The broken lines in (a) represent power laws obtained with a least square method applied to the jet data.

layers whose size varies with $\delta_i \sim L_0 Re_\lambda^{-1.4}$, we may estimate that N_{SH} increases with $(Re_\lambda^{-1.4})^{-3} = Re_\lambda^{4.2}$ because V_T is related to the width of the jet, which is also related to the length scale of large-scale motions L_0. In figure 17, N_{SH} increases with Re_λ. A least square method yields $N_{SH} \sim Re_\lambda^{3.9}$, which is not far from the above estimation. Here, the results shown in the figure do not consider the spatial variation of Re_λ as Re_λ is taken from the jet centreline. At least, the present shear layer detection method yields the Re_λ dependence of N_{SH} close to the estimation based on $\delta_i \sim L_0 Re_\lambda^{-1.4}$.

The mean intensities of the shear and biaxial strain of the shear layers are evaluated as $\overline{I_S}$ and $\overline{I_E}$ at $(\zeta_1, \zeta_2, \zeta_3) = (0, 0, 0)$. Figure 18$(a)$ presents $\overline{I_S}$ and $\overline{I_E}$ normalized by (u_0/L_0) as functions of the turbulent Reynolds number. The normalized shear and strain intensities agree well between the planar jet and homogeneous isotropic turbulence, and follow a power law of Re_λ. The power law exponents obtained by a least square method are -0.94 for $\overline{I_S}/(u_0/L_0)$ and -0.93 for $\overline{I_E}/(u_0/L_0)$ for the planar jet. Because of $(u_0/L_0) \sim (u_\eta/\eta) Re_\lambda^{-1}$, the power exponents close to -1 suggest that $\overline{I_S}/(u_\eta/\eta)$ and $\overline{I_E}/(u_\eta/\eta)$ hardly depend on Re_λ in these flows.

The Reynolds number of the shear layer can be defined as $Re_S = \Delta u_3 \delta_3/\nu$, which is based on the velocity jump of the shear and the layer thickness. Figure 18(b) plots Re_S against the turbulent Reynolds number in the planar jet and homogeneous isotropic

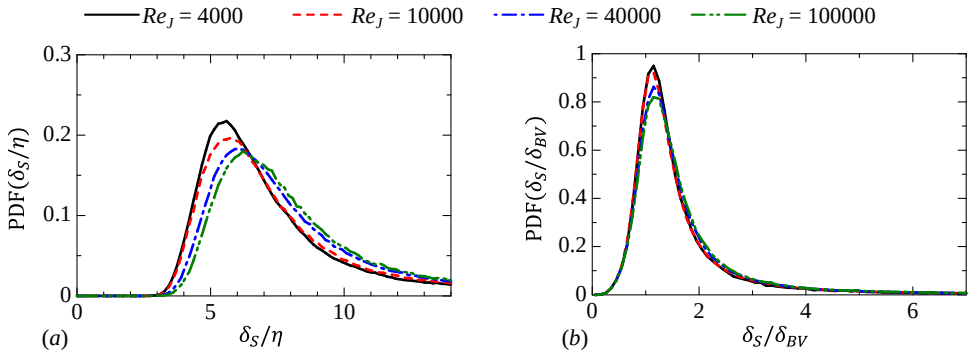

Figure 19: Probability density functions of shear layer thickness normalized by (*a*) Kolmogorov length scale η and (*b*) Burgers' vortex layer thickness δ_{BV} at $y = 0$.

turbulence. Although Re_S in each flow slowly increases with Re_λ, we obtain $Re_S \approx 45$ in the jet and $Re_S \approx 30$ in the homogeneous isotropic turbulence for a wide range of Re_λ. Weak Re_λ-dependence of Re_S is expected from the scaling of Δu_3 and δ_3. With the definitions of Re_S, η and u_η, Re_S can be rewritten as $Re_S = (\Delta u_3/u_\eta)(\delta_3/\eta)$. Therefore, Re_S does not depends on Re_λ when $\Delta u_3/u_\eta$ and δ_3/η are constant. Re_S is slightly larger in the planar jet than in homogeneous isotropic turbulence because $\Delta u_3/u_\eta$ is also larger in the jet. It is important to note that both flows have $Re_S \sim \mathcal{O}(10^1)$, which is high enough for the shear layers to become unstable (Beronov & Kida 1996), and the instability of the shear layers can result in the formation of vortex tubes in these flows.

The thickness of each shear layer can be estimated with the profile of I_S obtained for each local maximum of I_S. An instantaneous profile I_S on the ζ_2 axis has a peak at $\zeta_2 = 0$, and rapidly decreases as $|\zeta_2|$ becomes large. Therefore, the thickness of the shear layer δ_S is evaluated as the halfwidth of I_S on ζ_2. Namely, δ_S is the distance between two points on the ζ_2 axis with $I_S = I_{S,max}/2$ for $\zeta_2 > 0$ and $\zeta_2 < 0$, where $I_{S,max}$ is the value of I_S at $\zeta_2 = 0$. Figure 19(*a*) shows the PDF of δ_S normalized by η obtained at $y = 0$. The PDF for all Reynolds numbers has a peak at $\delta_S/\eta =$ 5-6. The instability of shear layers generates roller vortices, whose diameter is close to the shear layer thickness. The typical diameter of small-scale vortex tubes in a turbulent planar jet is about 7η (da Silva *et al.* 2011), which is close to the typical shear layer thickness 5-6η observed in the present DNS. This result also indicates that small-scale vortex tubes are produced by the instability of shear layers. In Burgers' vortex layer given by (4.2), the halfwidth of I_S is written with ν and I_E as $\delta_{BV} = 1.67\sqrt{4\nu/I_E}$. The thickness of shear layers in the DNS is compared with the prediction by Burgers' vortex layer. Here, for each local maxima of I_S, δ_{BV} is calculated with I_E at $(\zeta_1, \zeta_2, \zeta_3) = (0, 0, 0)$ while the actual halfwidth δ_S is also calculated from the profile of I_S on the ζ_2 axis. Figure 19(*b*) shows the PDF of δ_S/δ_{BV} obtained at $y = 0$. A large peak appears at $\delta_S/\delta_{BV} \approx 1$ for all Reynolds numbers. Thus, the shear layer thickness in the planar jet is well predicted by Burgers' vortex layer, which yields the thickness as a function of the intensity of the biaxial strain I_E and kinematic viscosity ν of the flow.

4.5. *Shear layers at different lateral positions in the jet*

The characteristics of shear layers are examined as functions of the lateral position of the planar jet. Here, the quantities related to the shear layers are normalized by the statistics calculated in the turbulent region with $\langle\ \rangle_T$. Figure 20(*a*) shows the velocity

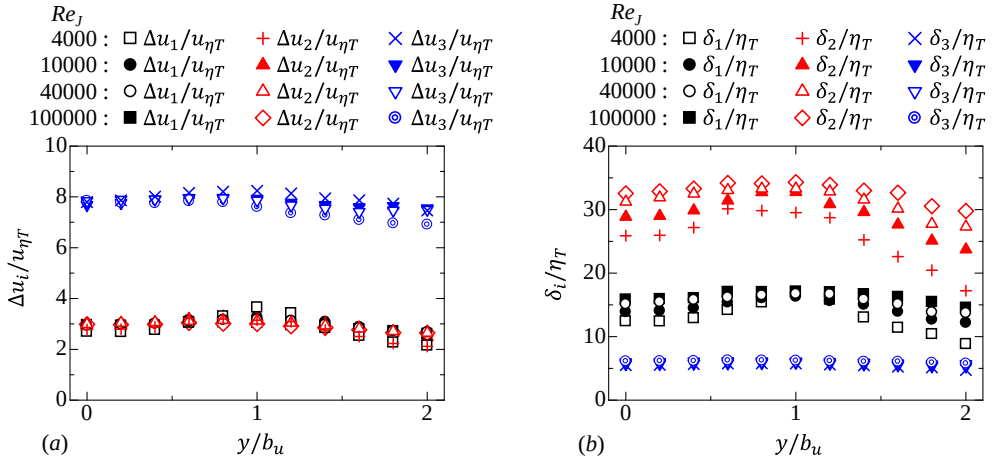

Figure 20: Lateral profiles of (*a*) $\Delta u_i/u_{\eta T}$ and (*b*) δ_i/η_T in the planar jet.

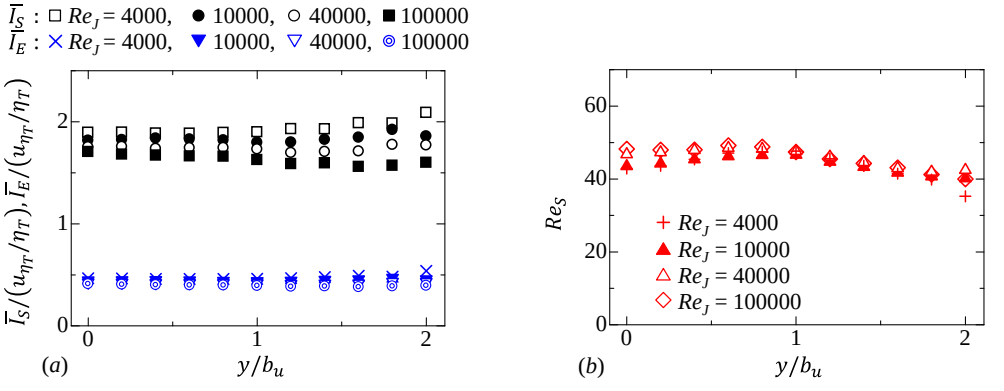

Figure 21: Lateral profiles of (*a*) $\overline{I_S}/(u_{\eta T}/\eta_T)$ and $\overline{I_E}/(u_{\eta T}/\eta_T)$ and (*b*) Re_S in the planar jet.

jumps Δu_i normalized by $u_{\eta T}$ as functions of y/b_u. The lateral profiles are similar for all Reynolds numbers. The planar jet has $\Delta u_1 \approx \Delta u_2 \approx 3u_{\eta T}$ and $\Delta u_3 \approx 8u_{\eta T}$, which weakly depend on y. Therefore, the velocity jumps of the shear layer at different lateral positions scale with the Kolmogorov velocity scale. Figure 20(*b*) plots the length scales of the shear layer, δ_i, normalized by η_T. The shear layer thickness δ_3 hardly depends on y when it is normalized by η_T, and the thickness is about $6\eta_T$ in the planar jet. On the other hand, variations of δ_1 and δ_2 across the jet are more noticeable than δ_3. The centre of the jet has $13 \lesssim \delta_1/\eta_T \lesssim 16$ and $25 \lesssim \delta_2/\eta_T \lesssim 33$ depending on the Reynolds number. δ_1/η_T and δ_2/η_T vary with y as much as with Re_J at $y = 0$. These variations are considered small because η_T/H used for the normalization changes between $\mathcal{O}(10^{-3})$ and $\mathcal{O}(10^{-4})$ depending on the Reynolds number, and the order of magnitude of δ_1/η_T and δ_2/η_T does not vary with y for all Reynolds numbers. δ_1 and δ_2 are related to a spatial extent of the region of the biaxial strain. In figure 20(*b*), the spatial variations of δ_1/η_T and δ_2/η_T with y occur over a distance of the order of b_u, which is one of the characteristic length scales of large-scale motions of the jet. Therefore, the profile of

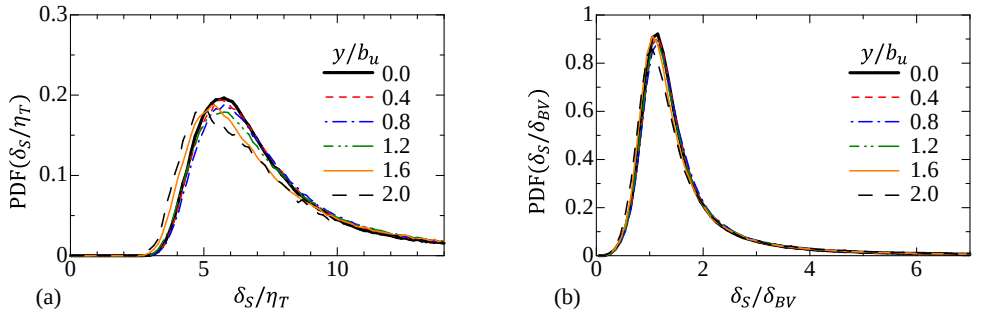

Figure 22: Probability density functions of shear layer thickness δ_S obtained at different lateral positions of the planar jet with $Re_J = 10000$. δ_S is normalized by (a) Kolmogorov length scale η_T and (b) Burgers' vortex layer thickness δ_{BV}.

δ_1/η_T and δ_2/η_T imply the possible influence of large-scale fluctuations on the biaxial strain acting on the small-scale shear layers.

Figure 21 shows the mean intensities of shear and elongation $\overline{I_S}$ and $\overline{I_E}$ and the shear Reynolds number Re_S, where $\overline{I_S}$ and $\overline{I_E}$ are evaluated at $(\zeta_1, \zeta_2, \zeta_3) = (0, 0, 0)$ and normalized by $(u_{\eta T}/\eta_T)$. These quantities hardly vary in the y direction. Therefore, the intensities of the shear and biaxial strain scale with the Kolmogorov scales in the planar jet. $Re_S \approx 40$ is also obtained across the planar jet for all Reynolds numbers examined in this study.

Figure 22 shows the PDF of δ_S/η_T and δ_S/δ_{BV} obtained at various lateral positions in the planar jet with $Re_J = 10000$. The PDF weakly depends on y, and the shear layer thickness normalized by the Kolmogorov length scale hardly changes with y. The peak of the PDF in figure 22(a) indicates that the typical thickness of the shear layers is about $6\eta_T$. Furthermore, the PDF of δ_S/δ_{BV} peaks at $\delta_S/\delta_{BV} \approx 1$, and the shear layer thickness is well predicted by Burgers' vortex layer in the planar jet.

Figure 23(a) shows the lateral profiles of the averages of three components of the shear vorticity, $\overline{(\boldsymbol{\omega}_S)_i}$, at the centre of the shear layer $(\zeta_1, \zeta_2, \zeta_3) = (0, 0, 0)$ for $Re_J = 10000$. In the planar jet, the mean shear $\partial\langle u\rangle/\partial y$ contributes to positive $\overline{(\boldsymbol{\omega}_S)_z}$. Therefore, $\overline{(\boldsymbol{\omega}_S)_z}$ becomes positive away from the jet centreline while $\overline{(\boldsymbol{\omega}_S)_x}$ and $\overline{(\boldsymbol{\omega}_S)_y}$ are close to 0. Figure 23(b) shows the PDF of $(\boldsymbol{\omega}_S)_z$ at the centre of the shear layer detected at $y/b_u = 0$ and 1. Because of the mean shear, the PDF at $y/b_u = 1$ is slightly shifted to positive $(\boldsymbol{\omega}_S)_z$. The sign of $(\boldsymbol{\omega}_S)_z$ represents the orientation of the shear in relation to the mean velocity gradient because the spanwise vorticity due to $\partial\langle u\rangle/\partial y$ is positive for $y > 0$. If the mean velocity gradient strongly affects the shear within the layer structures, the probability for $(\boldsymbol{\omega}_S)_z > 0$ should be much larger than that for $(\boldsymbol{\omega}_S)_z < 0$. However, the peak of the PDF appears at $(\boldsymbol{\omega}_S)_z \approx 0$ even at $y/b_u = 1$. In a turbulent boundary layer, the local velocity gradient across shear layers often has the same sign as the mean velocity gradient (Eisma *et al.* 2015). It should be noted that they used the two-dimensional triple decomposition, and three-dimensional features of the shear layers are not fully revealed. However, it seems that the mean shear effect on the shear layers is weaker in the turbulent planar jet than in the turbulent boundary layer. It is known that the mean streamwise velocity sharply changes near the interfacial layer between the turbulent and non-turbulent regions (TNTI layer) because the outside of the jet has small u (Westerweel *et al.* 2009). This mean velocity difference between the turbulent and non-turbulent regions may also affect the sign of $(\boldsymbol{\omega}_S)_z$ in the shear layers. The

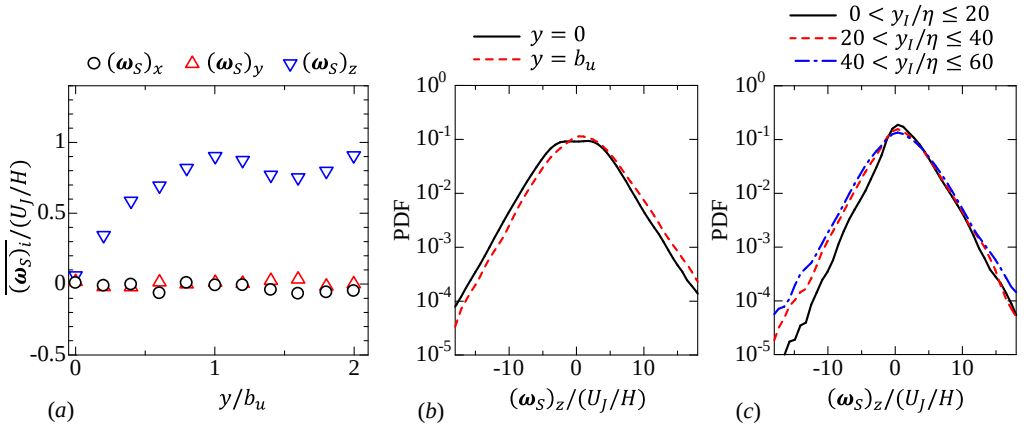

Figure 23: Statistics of shear vorticity $(\boldsymbol{\omega}_S)_i$ at the centre of the shear layers ($Re_J = 10000$). (a) Lateral profiles of the averages of shear vorticity components $\overline{(\boldsymbol{\omega}_S)_x}$, $\overline{(\boldsymbol{\omega}_S)_y}$ and $\overline{(\boldsymbol{\omega}_S)_z}$. ($b$) PDF of $(\boldsymbol{\omega}_S)_z$ of the shear layer detected at $y/b_u = 0$ and 1. (c) PDF of $(\boldsymbol{\omega}_S)_z$ of the shear layers which are located in $0 < y_I/\eta \leqslant 20$, $20 < y_I/\eta \leqslant 40$ or $40 < y_I/\eta \leqslant 60$. Here, y_I is the distance in the y direction from the shear layer to the isosurface of $\omega = \omega_{th}$ and η is taken at $y = 0$.

outer edge of the TNTI layer is well detected as the isosurface $\omega = \omega_{th}$. For the shear layer with the centre location given by (x_S, y_S, z_S), we examine the isosurface location y_ω in the y direction at $(x, z) = (x_S, z_S)$. We only consider the isosurface at $y > y_S$ because the shear layers are analysed for $y > 0$. The distance between the shear layer and the isosurface of $\omega = \omega_{th}$ is given by $y_I = y_\omega - y_S$, where the isosurface nearest to the shear layer is considered when the y axis crosses the isosurface more than once. The PDF of $(\boldsymbol{\omega}_S)_z$ is calculated for the shear layers located in three regions: $0 < y_I/\eta \leqslant 20$, $20 < y_I/\eta \leqslant 40$ and $40 < y_I/\eta \leqslant 60$. The TNTI layer is formed in $0 < y_I/\eta \lesssim 20$ in the temporally evolving planar jet (Silva *et al.* 2018). Figure 23(c) shows the PDF obtained in these regions. The probability for large negative $(\boldsymbol{\omega}_S)_z$ is noticeably small for $0 < y_I/\eta \leqslant 20$ compared with the other regions. The mean velocity jump near the TNTI layer contributes to positive $(\boldsymbol{\omega}_S)_z$, and low probability for $(\boldsymbol{\omega}_S)_z < 0$ in $0 < y_I/\eta \leqslant 20$ can be interpreted as the influence of the mean shear near the TNTI layer. However, the probability for $(\boldsymbol{\omega}_S)_z < 0$ is not zero, and the shear layers with the shear orientation opposite to the mean shear also appear even near the TNTI layer.

5. Conclusion

The characteristics of small-scale shear layers that internally exist in turbulent flows were studied with DNS of temporally evolving turbulent planar jets with the Reynolds number $Re_J = 4000, 10000$, 40000 and 100000. The velocity gradient tensor was decomposed into three components that represent motions of shear, rotation and elongation with the triple decomposition (Kolář 2007; Watanabe *et al.* 2020). In the turbulent planar jet, the shearing motion is stronger than the other motions. However, the motion of elongation becomes dominant far away from the jet centreline. The enstrophy production in the turbulent planar jet is dominated by the interaction between motions of shear and elongation as also found in homogeneous isotropic turbulence (Watanabe *et al.* 2020). Small-scale shear layers were identified as regions with strong shear. The shear layers

were analysed with averages taken around local maxima of the shear intensity I_S in the shear coordinate system, which was defined to express the shear with one component of the shear tensor.

The mean flow pattern around local maxima of I_S confirmed that a thin shear layer is formed in the region with biaxial strain, which consists of extensive strain in the direction of the vorticity vector of shear and compressive strain in the direction perpendicular to the shear layer. The velocity components associated with the shear and the compression of the biaxial strain rapidly change across the shear layer. Furthermore, the velocity component associated with the extensive strain also rapidly changes within the shear layer in the shear vorticity direction. This extensive strain can cause strong vortex stretching. The velocity jumps across the shear layers scale with the Kolmogorov velocity scale. The shear layer thickness normalized by the Kolmogorov scale also hardly changes with the Reynolds number. Furthermore, the intensities of the shear and biaxial strain of the shear layer also scale with the Kolmogorov scales. These quantities normalized by the Kolmogorov scales only weakly depend on the lateral position of the planar jet when the Kolmogorov scales are defined with averages of turbulent fluids. However, the length scales in the layer-parallel direction, δ_1 and δ_2, normalized by the Kolmogorov scale η_T slowly increase with Re_λ, and their variations across the planar jet are also larger than the shear layer thickness. The large variations of δ_1/η_T and δ_2/η_T imply that the biaxial strain acting on the shear layers is also influenced by large-scale velocity fluctuations in the planar jet. The spanwise component of shear vorticity $(\boldsymbol{\omega}_S)_z$ tends to have the same sign as the mean spanwise vorticity when the mean velocity gradient is not zero. A similar effect of the mean velocity gradient was also found within the interfacial layer between the turbulent and non-turbulent regions. However, there also exist a large number of the shear layers with $(\boldsymbol{\omega}_S)_z$ whose sign is opposite to the mean spanwise vorticity. Thus, the mean velocity gradient weakly affects the orientation of the shear layer, and the shear layers are associated with velocity fluctuations rather than the mean velocity gradient of the jet. The characteristics of shear layers normalized by the Kolmogorov scales show good agreement between the planar jet and homogeneous isotropic turbulence, and the small-scale shear layers have some universal properties that are independent of mean velocity gradients and Reynolds numbers.

Direct numerical simulations presented in this paper were performed using the high-performance computing system in the Japan Agency for Marine-Earth Science and Technology. This work was also supported by "Collaborative Research Project on Computer Science with High-Performance Computing in Nagoya University" and by JSPS KAKENHI Grant Number 20H05754.

Declaration of Interests

The authors report no conflict of interest

Appendix A. Identification of the basic reference frame of the triple decomposition

We use a method proposed in Nagata *et al.* (2020) to identify the basic reference frame, which is chosen from reference frames obtained with three sequential rotational transformations $\boldsymbol{Q}(\theta_1, \theta_2, \theta_3)$ with angles θ_i. The coordinate transformation tensor $\boldsymbol{Q}$ is

expressed as

$$\boldsymbol{Q} = \begin{pmatrix} \cos\theta_1\cos\theta_2\cos\theta_3 - \sin\theta_1\sin\theta_3 & \sin\theta_1\cos\theta_2\cos\theta_3 + \cos\theta_1\sin\theta_3 & -\sin\theta_2\cos\theta_3 \\ -\cos\theta_1\cos\theta_2\sin\theta_3 - \sin\theta_1\cos\theta_3 & -\sin\theta_1\cos\theta_2\sin\theta_3 + \cos\theta_1\cos\theta_3 & \sin\theta_2\sin\theta_3 \\ \cos\theta_1\sin\theta_2 & \sin\theta_1\sin\theta_2 & \cos\theta_2 \end{pmatrix}, \tag{A 1}$$

with the angles in the ranges of $0^\circ \leqslant \theta_1 \leqslant 180^\circ$, $0^\circ \leqslant \theta_2 \leqslant 180^\circ$ and $0^\circ \leqslant \theta_3 \leqslant 90^\circ$. In the basic reference frame, the shear intensity $I_S = \sqrt{2(\nabla \boldsymbol{u}_S)_{ij}(\nabla \boldsymbol{u}_S)_{ij}}$ takes the largest value among all possible reference frames. Hereafter, superscript $*$ represents a tensor evaluated in the rotated reference frame defined with $\boldsymbol{Q}$. For example, the velocity gradient tensor in the rotated frame is calculated as $(\nabla \boldsymbol{u})^* = \boldsymbol{Q}\,(\nabla \boldsymbol{u})\,\boldsymbol{Q}^T$. The basic reference frame is identified with the following procedures.

(i) Apply the coordinate transformation (A 1) to $\nabla \boldsymbol{u}$ with all sets of $(\theta_1, \theta_2, \theta_3)$ given by

$$\theta_1 = 0, 45^\circ, 90^\circ, \ldots, 180^\circ, \tag{A 2}$$
$$\theta_2 = 0, 45^\circ, 90^\circ, \ldots, 180^\circ, \tag{A 3}$$
$$\theta_3 = 0, 45^\circ, 90^\circ, \tag{A 4}$$

where the angles are discretely changed by 45°. Calculate $I_S = \sqrt{2(\nabla \boldsymbol{u}_S)^*_{ij}(\nabla \boldsymbol{u}_S)^*_{ij}}$ in the rotated reference frames with $(\nabla \boldsymbol{u}_S)^*_{ij}$ obtained by (3.1).

(ii) Find $(\theta_1, \theta_2, \theta_3)$ which gives the maximum I_S among the rotated reference frames considered in (i). These angles with the maximum I_S are denoted by $(\theta_1^{(1)}, \theta_2^{(1)}, \theta_3^{(1)})$.

(iii) Apply (A 1) to $\nabla \boldsymbol{u}$ with all sets of $(\theta_1, \theta_2, \theta_3)$ given by

$$\theta_1 = \theta_1^{(1)} - 45^\circ/2,\ \theta_1^{(1)} - 45^\circ/2 + 15^\circ, \ldots, \theta_1^{(1)} + 45^\circ/2, \tag{A 5}$$
$$\theta_2 = \theta_2^{(1)} - 45^\circ/2,\ \theta_2^{(1)} - 45^\circ/2 + 15^\circ, \ldots, \theta_2^{(1)} + 45^\circ/2, \tag{A 6}$$
$$\theta_3 = \theta_3^{(1)} - 45^\circ/2,\ \theta_3^{(1)} - 45^\circ/2 + 15^\circ, \ldots, \theta_3^{(1)} + 45^\circ/2, \tag{A 7}$$

where the angles are discretely changed by 15°.

(iv) Find $(\theta_1, \theta_2, \theta_3)$ which gives the maximum $I_S = \sqrt{2(\nabla \boldsymbol{u}_S)^*_{ij}(\nabla \boldsymbol{u}_S)^*_{ij}}$ among the rotated reference frames considered in (iii). The angles for the maximum I_S are denoted by $(\theta_1^{(2)}, \theta_2^{(2)}, \theta_3^{(2)})$.

(v) Apply (A 1) to $\nabla \boldsymbol{u}$ with all sets of $(\theta_1, \theta_2, \theta_3)$ given by

$$\theta_1 = \theta_1^{(2)} - 15^\circ/2,\ \theta_1^{(2)} - 15^\circ/2 + 5^\circ, \ldots, \theta_1^{(2)} + 15^\circ/2, \tag{A 8}$$
$$\theta_2 = \theta_2^{(2)} - 15^\circ/2,\ \theta_2^{(2)} - 15^\circ/2 + 5^\circ, \ldots, \theta_2^{(2)} + 15^\circ/2, \tag{A 9}$$
$$\theta_3 = \theta_3^{(2)} - 15^\circ/2,\ \theta_3^{(2)} - 15^\circ/2 + 5^\circ, \ldots, \theta_3^{(2)} + 15^\circ/2, \tag{A 10}$$

where the angles are discretely changed by 5°.

(vi) The basic reference frame is defined with the angles that yield the maximum $I_S = \sqrt{2(\nabla \boldsymbol{u}_S)^*_{ij}(\nabla \boldsymbol{u}_S)^*_{ij}}$ among the rotated reference frames considered in (v).

The angle 5° is small enough to accurately identify the basic reference frame, and the results of the decomposition hardly change with such small $\Delta^{(3)}$ as confirmed in Nagata

et al. (2020). The above procedure is applied to $\nabla \boldsymbol{u}$ at each grid point of DNS and is repeated to obtain the basic reference frames in the entire computational domain.

Appendix B. Identification of the shear coordinate

The shear coordinate that satisfies (3.15) and (3.16) is identified by the method proposed in Watanabe *et al.* (2020), and this method is briefly described here. The shear coordinate is described by three orthogonal unit vectors $\boldsymbol{n}_1$, $\boldsymbol{n}_2$ and $\boldsymbol{n}_3$, which are chosen from $(N_n + 1)$ candidates of the x component of $\boldsymbol{n}_2$, $(\boldsymbol{n}_2)_x$. We assume $(\boldsymbol{n}_2)_x = 2(n/N_n - 0.5)$ with an integer $n = 0, ..., N_n$. The present study uses $N_n = 4000$ because the results presented in this paper do not change with such large N_n. In the present analysis, $\boldsymbol{n}_2$ and $\boldsymbol{n}_3$ that define the shear coordinate are determined from a large number of orthogonal coordinates obtained with $n = 0, ..., N_n$. $\boldsymbol{n}_1$ is already determined as the direction of the vorticity vector of the shear tensor, $\boldsymbol{n}_1 = \boldsymbol{\omega}_S/|\boldsymbol{\omega}_S|$. For each n that yields $(\boldsymbol{n}_2)_x = 2(n/N_n - 0.5)$, the remaining components of the unit vectors, $(\boldsymbol{n}_2)_y$, $(\boldsymbol{n}_2)_z$ and $\boldsymbol{n}_3$ are calculated from three conditions: orthogonality of $(\boldsymbol{n}_1, \boldsymbol{n}_2, \boldsymbol{n}_3)$, unit vectors $|\boldsymbol{n}_i| = 1$ and right-hand system. Some values of n do not yield the orthogonal coordinate under the above condition. These values of n are discarded from the following analysis. The shear coordinate is obtained by $\boldsymbol{\zeta} = \boldsymbol{Q}_\zeta \boldsymbol{x}$ with the transformation tensor $\boldsymbol{Q}_\zeta$ defined with $\boldsymbol{n}_i$. The shear tensor in the coordinate system $\boldsymbol{\zeta}$ is calculated as $\boldsymbol{Q}_\zeta(\nabla \boldsymbol{u}_S)\boldsymbol{Q}_\zeta^T$. The conditions of (3.15) and (3.16) are satisfied the best among $n = 1, ..., N_n$ for n that yields the maximum value of $(\nabla \boldsymbol{u}_S)_{32}$ after the coordinate transformation. This value of n yields $\boldsymbol{n}_2$ and $\boldsymbol{n}_3$ used to define the shear coordinate.

The shear coordinate is not unique because the coordinate defined with $(\boldsymbol{n}_1, \boldsymbol{n}_2, \boldsymbol{n}_3)$ has the same physical meaning as the one defined with the unit vectors obtained by inverting the directions of two components of $(\boldsymbol{n}_1, \boldsymbol{n}_2, \boldsymbol{n}_3)$. In this study, we only consider the shear coordinate with $(\boldsymbol{n}_2)_y > 0$ by excluding values of n that yield negative $(\boldsymbol{n}_2)_y$. This constraint avoids the ambiguity of the shear coordinate. The shear layers found for $y > 0$ are analysed in this study, and $(\boldsymbol{n}_2)_y > 0$ means that the $(\boldsymbol{n}_2)_y$ is oriented in the outward direction of the jet. A similar method was used to define the reference frame of eigenvectors of the rate-of-strain tensor in a turbulent jet because the reference frame defined with the eigenvectors is also not unique for the same reason (Elsinga & da Silva 2019). They used the vorticity direction and the direction perpendicular to the turbulent/non-turbulent interface to define the reference frame without ambiguity.

REFERENCES

Attili, A., Cristancho, J. C. & Bisetti, F. 2014 Statistics of the turbulent/non-turbulent interface in a spatially developing mixing layer. *J. Turbulence* **15** (9), 555–568.

Balaras, E., Piomelli, U. G. O. & Wallace, J. M. 2001 Self-similar states in turbulent mixing layers. *Journal of Fluid Mechanics* **446**, 1.

Beronov, K. N. & Kida, S. 1996 Linear two-dimensional stability of a Burgers vortex layer. *Phys. Fluids* **8** (4), 1024–1035.

Bisset, D. K., Hunt, J. C. R. & Rogers, M. M. 2002 The turbulent/non-turbulent interface bounding a far wake. *J. Fluid Mech.* **451**, 383–410.

Cafiero, G. & Vassilicos, J. C. 2020 Non-equilibrium scaling of the turbulent-nonturbulent interface speed in planar jets. *Phys. Rev. Lett.* **125** (17), 174501.

Davidson, P. A. 2004 *Turbulence: An Introduction for Scientists and Engineers*. Oxford Univ. Pr.

Deo, R. C., Mi, J. & Nathan, G. J. 2008 The influence of Reynolds number on a plane jet. *Phys. Fluids* **20** (7), 075108.

Deo, R. C., Nathan, G. J. & Mi, J. 2013 Similarity analysis of the momentum field of a

subsonic, plane air jet with varying jet-exit and local Reynolds numbers. *Phys. Fluids* **25** (1), 015115.

Diamessis, P. J., Spedding, G. R. & Domaradzki, J. A. 2011 Similarity scaling and vorticity structure in high-Reynolds-number stably stratified turbulent wakes. *J. Fluid Mech.* **671**, 52–95.

Eisma, J., Westerweel, J., Ooms, G. & Elsinga, G. E. 2015 Interfaces and internal layers in a turbulent boundary layer. *Phys. Fluids* **27** (5), 055103.

Elsinga, G. E. & da Silva, C. B. 2019 How the turbulent/non-turbulent interface is different from internal turbulence. *J. Fluid Mech.* **866**, 216–238.

Gampert, M., Boschung, J., Hennig, F., Gauding, M. & Peters, N. 2014 The vorticity versus the scalar criterion for the detection of the turbulent/non-turbulent interface. *J. Fluid Mech.* **750**, 578–596.

Ghanem, A., Lemenand, T., Della Valle, D. & Peerhossaini, H. 2014 Static mixers: Mechanisms, applications, and characterization methods–A review. *Chem. Eng. Res. Des.* **92** (2), 205–228.

Gul, M., Elsinga, G. E. & Westerweel, J. 2020 Internal shear layers and edges of uniform momentum zones in a turbulent pipe flow. *J. Fluid Mech.* **901**.

Gutmark, E & Wygnanski, I 1976 The planar turbulent jet. *J. Fluid Mech.* **73**, 465–495.

Horiuti, K. 2001 A classification method for vortex sheet and tube structures in turbulent flows. *Phys. Fluids* **13** (12), 3756–3774.

Horiuti, K. & Takagi, Y. 2005 Identification method for vortex sheet structures in turbulent flows. *Phys. Fluids* **17** (12), 121703.

Jahanbakhshi, R., Vaghefi, N. S. & Madnia, C. K. 2015 Baroclinic vorticity generation near the turbulent/non-turbulent interface in a compressible shear layer. *Phys. Fluids* **27** (10), 105105.

Jimenez, J. & Wray, A. A. 1998 On the characteristics of vortex filaments in isotropic turbulence. *J. Fluid Mech.* **373**, 255–285.

Jiménez, J., Wray, A. A., Saffman, P. G. & Rogallo, R. S. 1993 The structure of intense vorticity in isotropic turbulence. *J. Fluid Mech.* **255**, 65–90.

Kang, S.-J., Tanahashi, M. & Miyauchi, T. 2007 Dynamics of fine scale eddy clusters in turbulent channel flows. *J. Turbul.* (8), N52.

Kholmyansky, M., Tsinober, A. & Yorish, S. 2001 Velocity derivatives in the atmospheric surface layer at $re_\lambda = 10^4$. *Phys. Fluids* **13** (1), 311–314.

Klein, M., Sadiki, A. & Janicka, J. 2003 Investigation of the influence of the Reynolds number on a plane jet using direct numerical simulation. *Int. J. Heat Fluid Flow* **24** (6), 785–794.

Kolář, V. 2007 Vortex identification: New requirements and limitations. *Int. J. Heat Fluid Flow* **28** (4), 638–652.

Kozul, M., Chung, D. & Monty, J. P. 2016 Direct numerical simulation of the incompressible temporally developing turbulent boundary layer. *J. Fluid Mech.* **796**, 437–472.

LaRue, J. C. & Libby, P. A. 1974 Temperature fluctuations in the plane turbulent wake. *Phys. Fluids* **17** (11), 1956–1967.

Maciel, Y., Robitaille, M. & Rahgozar, S. 2012 A method for characterizing cross-sections of vortices in turbulent flows. *Int. J. Heat Fluid flow* **37**, 177–188.

Matsubara, M., Alfredsson, P. H. & Segalini, A. 2020 Linear modes in a planar turbulent jet. *J. Fluid Mech.* **888**.

Meneveau, C. 2011 Lagrangian dynamics and models of the velocity gradient tensor in turbulent flows. *Annu. Rev. Fluid Mech.* **43**, 219–245.

Morinishi, Y., Lund, T. S., Vasilyev, O. V. & Moin, P. 1998 Fully conservative higher order finite difference schemes for incompressible flow. *J. Comput. Phys.* **143** (1), 90–124.

Moser, R. D, Rogers, M. M. & Ewing, D. W. 1998 Self-similarity of time-evolving plane wakes. *J. Fluid Mech.* **367**, 255–289.

Nagata, R., Watanabe, T., Nagata, K. & da Silva, C. B. 2020 Triple decomposition of velocity gradient tensor in homogeneous isotropic turbulence. *Comput. Fluids* **198**, 104389.

Namer, I. & Ötügen, M. V. 1988 Velocity measurements in a plane turbulent air jet at moderate Reynolds numbers. *Exp. Fluids* **6** (6), 387–399.

Pirozzoli, S., Bernardini, M. & Grasso, F. 2008 Characterization of coherent vortical structures in a supersonic turbulent boundary layer. *J. Fluid Mech.* **613**, 205.

Pirozzoli, S., Bernardini, M. & Grasso, F. 2010 On the dynamical relevance of coherent vortical structures in turbulent boundary layers. *J. Fluid Mec.* **648**, 325.

Pope, S. B. 2000 *Turbulent Flows*. Cambridge Univ. Pr.

van Reeuwijk, M. & Holzner, M. 2014 The turbulence boundary of a temporal jet. *J. Fluid Mech.* **739**, 254–275.

Rogers, M. M. & Moser, R. D. 1994 Direct simulation of a self-similar turbulent mixing layer. *Phys. Fluids* **6** (2), 903–923.

Ruetsch, G. R. & Maxey, M. R. 1991 Small-scale features of vorticity and passive scalar fields in homogeneous isotropic turbulence. *Phys. Fluids* **3** (6), 1587–1597.

Sadeghi, H., Oberlack, M. & Gauding, M. 2018 On new scaling laws in a temporally evolving turbulent plane jet using Lie symmetry analysis and direct numerical simulation. *J Fluid Mech.* **854**, 233–260.

Siggia, E. D. 1981 Numerical study of small-scale intermittency in three-dimensional turbulence. *J. Fluid Mech.* **107**, 375–406.

da Silva, C. B., Dos Reis, R. J. N. & Pereira, J. C. F. 2011 The intense vorticity structures near the turbulent/non-turbulent interface in a jet. *J. Fluid Mech.* **685**, 165–190.

da Silva, C. B., Hunt, J. C. R., Eames, I. & Westerweel, J. 2014 Interfacial layers between regions of different turbulence intensity. *Annu. Rev. Fluid Mech.* **46**, 567–590.

da Silva, C. B. & Lopes, D. C.and Raman, V. 2015 The effect of subgrid-scale models on the entrainment of a passive scalar in a turbulent planar jet. *J. Turbul.* **16** (4), 342–366.

da Silva, C. B. & Pereira, J. C. F. 2008 Invariants of the velocity-gradient, rate-of-strain, and rate-of-rotation tensors across the turbulent/nonturbulent interface in jets. *Phys. Fluids* **20** (5), 055101.

Silva, T. S., Zecchetto, M. & da Silva, C. B. 2018 The scaling of the turbulent/non-turbulent interface at high Reynolds numbers. *J. Fluid Mech.* **843**, 156.

Stanley, S. A., Sarkar, S. & Mellado, J. P. 2002 A study of the flow-field evolution and mixing in a planar turbulent jet using direct numerical simulation. *J. Fluid Mech.* **450**, 377–407.

Takahashi, M., Iwano, K., Sakai, Y. & Ito, Y. 2019 Experimental investigation on destruction of Reynolds stress in a plane jet. *Exp. Fluids* **60** (3), 1–15.

Taveira, R. R., Diogo, J. S., Lopes, D. C. & da Silva, C. B. 2013 Lagrangian statistics across the turbulent-nonturbulent interface in a turbulent plane jet. *Phys. Rev. E* **88** (4), 043001.

Taveira, R. R. & da Silva, C. B. 2013 Kinetic energy budgets near the turbulent/nonturbulent interface in jets. *Phys. Fluids* **25**, 015114.

Terashima, O., Sakai, Y. & Ito, Y. 2018 Measurement of fluctuating temperature and POD analysis of eigenmodes in a heated planar jet. *Exp. Therm. Fluid Sci.* **92**, 113–124.

Terashima, O., Sakai, Y. & Nagata, K. 2012 Simultaneous measurement of velocity and pressure in a plane jet. *Exp. Fluids* **53** (4), 1149–1164.

Thiesset, F., Schaeffer, V., Djenidi, L. & Antonia, R. A. 2014 On self-preservation and log-similarity in a slightly heated axisymmetric mixing layer. *Phys. Fluids* **26** (7), 075106.

Tsinober, A. 2009 *An informal conceptual introduction to turbulence*. Springer.

Veynante, D. & Vervisch, L. 2002 Turbulent combustion modeling. *Prog. Energy Combust. Sci.* **28** (3), 193–266.

Vincent, A. & Meneguzzi, M. 1994 The dynamics of vorticity tubes in homogeneous turbulence. *J. Fluid Mech.* **258**, 245–254.

Watanabe, T., Naito, T., Sakai, Y., Nagata, K. & Ito, Y. 2015 Mixing and chemical reaction at high schmidt number near turbulent/nonturbulent interface in planar liquid jet. *Phys. Fluids* **27** (3), 035114.

Watanabe, T., Riley, J. J., Nagata, K., Onishi, R. & Matsuda, K. 2018*a* A localized turbulent mixing layer in a uniformly stratified environment. *J. Fluid Mech.* **849**, 245–276.

Watanabe, T., Sakai, Y., Nagata, K., Ito, Y. & Hayase, T. 2014*a* Enstrophy and passive scalar transport near the turbulent/non-turbulent interface in a turbulent planar jet flow. *Phys. Fluids* **26** (10), 105103.

Watanabe, T., Sakai, Y., Nagata, K., Ito, Y. & Hayase, T. 2014*b* Vortex stretching and compression near the turbulent/nonturbulent interface in a planar jet. *J. Fluid Mech.* **758**, 754–785.

Watanabe, T., Sakai, Y., Nagata, K. & Terashima, O. 2014*c* Experimental study on the reaction rate of a second-order chemical reaction in a planar liquid jet. *AIChE J.* **60** (11), 3969–3988.

Watanabe, T., da Silva, C. B., Nagata, K. & Sakai, Y. 2017 Geometrical aspects of turbulent/non-turbulent interfaces with and without mean shear. *Phys. Fluids* **29** (8), 085105.

Watanabe, T., Tanaka, K. & Nagata, K. 2020 Characteristics of shearing motions in incompressible isotropic turbulence. *Phys. Rev. Fluids* **5** (7), 072601.

Watanabe, T., Zhang, X. & Nagata, K. 2018*b* Turbulent/non-turbulent interfaces detected in DNS of incompressible turbulent boundary layers. *Phys. Fluids* **30** (3), 035102.

Watanabe, T., Zhang, X. & Nagata, K. 2019 Direct numerical simulation of incompressible turbulent boundary layers and planar jets at high Reynolds numbers initialized with implicit large eddy simulation. *Comput. Fluids* **194**, 104314.

Westerweel, J., Fukushima, C., Pedersen, J. M. & Hunt, J. C. R. 2009 Momentum and scalar transport at the turbulent/non-turbulent interface of a jet. *J. Fluid Mech.* **631**, 199–230.

Wu, N., Sakai, Y., Nagata, K., Suzuki, H., Terashima, O. & Hayase, T. 2013 Analysis of flow characteristics of turbulent plane jets based on velocity and scalar fields using DNS. *J. Fluid Sci. Tech.* **8** (3), 247–261.

Yamamoto, K. & Hosokawa, I. 1988 A decaying isotropic turbulence pursued by the spectral method. *J. Phys. Soc. Japan* **57** (5), 1532–1535.

Zhou, Y. & Vassilicos, J. C. 2017 Related self-similar statistics of the turbulent/non-turbulent interface and the turbulence dissipation. *J. Fluid Mech.* **821**, 440–457.